



1 **AWARE: The Atmospheric Radiation Measurement (ARM) West Antarctic Radiation**
2 **Experiment**

3
4 Dan Lubin¹, Damao Zhang², Israel Silber³, Ryan C. Scott¹, Petros Kalogeras⁴, Alessandro
5 Battaglia⁴, David H. Bromwich⁵, Maria Cadetdu⁶, Edwin Eloranta⁷, Ann Fridlind⁸, Amanda
6 Frossard⁹, Keith M. Hines⁵, Stefan Kneifel¹⁰, W. Richard Leaitch¹¹, Wuyin Lin², Julien
7 Nicolas¹², Heath Powers¹³, Patricia K. Quinn¹⁴, Penny Rowe^{15,16}, Lynn M. Russell¹, Sangeeta
8 Sharma¹¹, Johannes Verlinde³, and Andrew M. Vogelmann²

9
10 ¹Scripps Institution of Oceanography, La Jolla, CA

11 ²Brookhaven National Laboratory, Upton, NY

12 ³Pennsylvania State University, University Park, PA

13 ⁴University of Leicester, Leicester, United Kingdom

14 ⁵Byrd Polar and Climate Research Center, Columbus, OH

15 ⁶Argonne National Laboratory, Lemont, IL

16 ⁷University of Wisconsin, Madison, WI

17 ⁸NASA Goddard Institute for Space Studies, New York, NY

18 ⁹University of Georgia, Athens, GA

19 ¹⁰University of Cologne, Cologne, Germany

20 ¹¹Environment and Climate Change Canada, Toronto, Canada

21 ¹²European Centre for Medium-Range Weather Forecasts, Reading, United Kingdom

22 ¹³Los Alamos National Laboratory, Los Alamos, NM

23 ¹⁴NOAA Pacific Marine Environmental Laboratory, Seattle, WA

24 ¹⁵NorthWest Research Associates, Redmond, WA

25 ¹⁶University of Santiago, Santiago, Chile

26

27 Submitted to *Bulletin of the American Meteorological Society*, revised 14 December 2019

28

29 Corresponding Author: Dan Lubin, Scripps Institution of Oceanography, University of California
30 San Diego, La Jolla, CA 92093-0221, USA. Email: dlubin@ucsd.edu

31

Early Online Release: This preliminary version has been accepted for publication in *Bulletin of the American Meteorological Society*, may be fully cited, and has been assigned DOI 10.1175/BAMS-D-18-0278.1. The final typeset copyedited article will replace the EOR at the above DOI when it is published.

32 **Capsule Summary**

33 The ARM West Antarctic Radiation Experiment, a joint US Department of Energy and US
34 Antarctic Program field campaign, collected a full year of atmospheric and remote sensing data
35 that reveal significant contrasts with Arctic data in meteorology, cloud physics and aerosol
36 chemical composition, and which have unique value for development and validation of climate
37 models.

38

39 **Abstract**

40 The US Department of Energy Atmospheric Radiation Measurement (ARM) West
41 Antarctic Radiation Experiment (AWARE) performed comprehensive meteorological and aerosol
42 measurements, and ground-based atmospheric remote sensing at two Antarctic stations using the
43 most advanced instrumentation available. A suite of cloud research radars, lidars, spectral and
44 broadband radiometers, aerosol chemical and microphysical sampling equipment, and
45 meteorological instrumentation was deployed at McMurdo Station on Ross Island from December
46 2015 through December 2016. A smaller suite of radiometers and meteorological equipment
47 including radiosondes, optimized for surface energy budget measurement, was deployed on the
48 West Antarctic Ice Sheet between 4 December 2015 and 17 January 2016. AWARE provided
49 Antarctic atmospheric data comparable to several well-instrumented high Arctic sites that have
50 operated for many years and that reveal numerous contrasts with the Arctic in aerosol and cloud
51 microphysical properties. These include persistent differences in liquid cloud occurrence, cloud
52 height and cloud thickness. Antarctic aerosol properties are also quite different from the Arctic in
53 both seasonal cycle and composition, due to the continent's isolation from lower latitudes by
54 Southern Ocean storm tracks. Antarctic aerosol number and mass concentrations are not only non-

55 negligible but perhaps play a more important role than previously recognized because of the higher
56 sensitivities of clouds at the very low concentrations caused by the large-scale dynamical isolation.
57 Antarctic aerosol chemical composition, particularly organic components, has implications for
58 local cloud microphysics. The AWARE data set, fully available online in the ARM Program data
59 archive, offers numerous case studies for unique and rigorous evaluation of mixed-phase cloud
60 parameterization in climate models.

61

62 **Introduction**

63 West Antarctica is one of the most rapidly warming regions on Earth, and this warming is
64 closely connected with global sea level rise. The discovery of rapid climate change on the West
65 Antarctic Ice Sheet (WAIS) has challenged previous explanations of Antarctic climate change that
66 focused on strengthening of circumpolar westerlies in response to the positive polarity trend in the
67 Southern Annular Mode (Bromwich et al. 2013; Nicolas and Bromwich 2014). West Antarctic
68 warming trends do not yet have a comprehensive explanation. Dynamical mechanisms may vary
69 from one season to the next, and these mechanisms very likely involve complex teleconnections
70 with subtropical and tropical latitudes (e.g., Ding et al. 2011; Schneider et al. 2012). Field work
71 for atmospheric and climate science has historically been sparse due to logistical challenges
72 (Bromwich et al. 2012), especially for West Antarctica where the areas of greatest interest for sea
73 level rise are very distant from the major or permanent field stations of any nation's Antarctic
74 program. Direct meteorological information on the WAIS has mostly been limited to a few
75 automatic weather stations (AWS) for several decades (Lazzara et al. 2012). And yet satellite
76 imagery, measurements and meteorological reanalyses indicate that West Antarctica is highly
77 susceptible to advection of warm and moist maritime air, with related cloud cover, depending on

78 the location and strength of low pressure centers in the Amundsen, Ross, and Bellingshausen Seas
79 (Jolly et al. 2018; Nicolas and Bromwich 2011). At the same time, satellite profiling, even with
80 active sensors, often misses important details regarding clouds and precipitation in the Antarctic
81 lower troposphere (e.g., Maahn et al. 2014), and this further emphasizes the need for
82 comprehensive surface-based measurements. Recently, Scott et al. (2019) have linked surface
83 melting conditions on the WAIS to blocking activity in the Amundsen Sea region and to a negative
84 phase of the Southern Annular Mode, both of which correlate with El Niño conditions in the
85 tropical Pacific Ocean. There is a need to quantify the role of these changing air masses on the
86 surface energy balance (SEB), including all surface energy components and cloud radiative forcing
87 (e.g., Bromwich et al. 2012; Trenberth and Fasullo 2010; Hyder et al. 2019; Silber et al. 2019a).
88 More generally, global climate model simulations are known to perform poorly over the Antarctic
89 and Southern Ocean (e.g., Trenberth and Fasullo 2010; Hyder et al. 2019), and the relative scarcity
90 of cloud information at Southern high latitudes has so far inhibited progress.

91 Surface melt conditions during summer are increasingly realized to have a potentially
92 important role in WAIS mass loss. Analysis of satellite and aerial photographic observations by
93 Kingslake et al. (2017) reveals how extensively and frequently surface melt conditions can occur
94 throughout lower-elevation regions of Antarctica. The largest immediate cause of ice sheet
95 acceleration in West Antarctica is recognized to be ice shelf thinning via basal melting from a
96 warming ocean (Pritchard et al. 2012; Paolo et al. 2015). Concurrent with this ocean-induced ice
97 shelf loss is retreat of the grounding line (the transition between the ice sheet and floating ice shelf)
98 throughout West Antarctica (Rignot et al. 2014). Once stabilization by ice shelf buttressing is lost
99 (Fürst et al. 2016), ice sheet acceleration in West Antarctica is potentially rapid due to the
100 underlying topography that slopes downward as one goes inland. This is the well-known marine

101 ice sheet instability (MISI; Weertman 1974; Oppenheimer 1998; Alley et al. 2015). A MISI-related
102 collapse may have already started for the Thwaites Glacier basin (Joughin et al. 2014).

103 However, the major role of oceanic warming in West Antarctica does not signify that direct
104 atmospheric warming is a negligible factor. Pollard et al. (2015) and DeConto and Pollard (2016)
105 have identified a marine ice cliff instability (MICI) that operates in conjunction with the MISI.
106 When surface air temperatures approach and exceed freezing, surface melt water filtering into
107 crevasses can induce hydrofracturing near the grounding line, weakening the grounded ice column
108 at its edge and increasing the calving rate (see also Bassis and Jacobs 2013). Hydrofracturing will
109 also occur on the ice shelves themselves, further increasing their loss rate and exposing these
110 unstable ice cliffs at the grounding line (DeConto and Pollard 2016). The three over-arching
111 processes in cryosphere mass loss are direct melt runoff, glacier and ice sheet calving, and ice shelf
112 ablation through basal melting. The difference between the net of these processes and
113 accumulation defines the mass balance of the cryosphere (Zwally et al. 2005). These three
114 processes are also inter-related. For example, on grounded ice sheets, melt water can accelerate
115 ice sheet motion and calving by (1) filtering down to the base of the ice sheet and lubricating its
116 downslope motion; and (2) hydrofracturing, in which surface meltwater ponds and infiltrates
117 crevasses, acting as a slow-motion “jackhammer” that weakens an ice shelf structure (e.g.,
118 Scambos et al. 2000).

119 All three of these processes play important roles in Greenland (e.g., Fürst et al. 2015). In
120 Antarctica, we are mainly concerned about the stability of systems of moving ice sheets partially
121 buttressed by their adjacent and attached floating ice shelves. Fürst et al. (2016) demonstrate that
122 ice shelf buttressing plays a critical role in the stability of ice sheets adjacent to the Amundsen and
123 Bellingshausen Seas. Moreover, the recent work of Pollard et al. (2015) and DeConto and Pollard

124 (2016) indicates an important role for direct atmospheric forcing on ice shelf hydrofracturing in
125 West Antarctica. Parameterizations for ice shelf hydrofracturing and the MICI in coupled climate
126 models are still in their early stages; actual field data are required for model testing and refinement,
127 and for attribution of surface melting events to specific atmospheric processes such as warm air
128 intrusion (Nicolas and Bromwich 2011; Scott et al. 2019), cloud all-wave surface radiation
129 enhancement (Bennartz et al. 2013; Hu et al. 2019), or foehn winds (e.g., Elvidge et al. 2015; Zhou
130 et al. 2019).

131 AWARE is an effort to acquire critical atmospheric data to fundamentally understand
132 atmospheric forcing on West Antarctica, and to foster related improvements to climate model
133 performance. Within the past two decades other regions of the Antarctic continent have seen
134 several field campaigns and growing permanent installations of advanced atmospheric science
135 equipment, all of which are providing new insights into the continent's unique meteorology and
136 climatology. Two of the most persistent efforts have occurred on the high plateau of East
137 Antarctica: (1) at the South Pole with Fourier Transform Infrared (FTIR) spectroradiometer
138 measurements (e.g., Walden et al. 2006; Town et al. 2007), and micropulse lidar (MPL)
139 combined with tethered balloon cloud microphysical observations (Lawson and Gettelman
140 2014); and (2) multi-sensor observations of ice clouds over Dome C that include multispectral
141 microwave radiometry (Ricaud et al. 2017). Research radars for cloud and precipitation recently
142 deployed at Dumont d'Urville Station in Adélie Land have revealed how katabatic outflows
143 sublimate precipitation, thus impacting the long-term ice mass balance (Grazioli et al. 2017). A
144 climate observatory has been established at Princess Elizabeth Base in Queen Maud Land, East
145 Antarctica, that presently maintains a precipitation radar along with comprehensive
146 meteorological measurements whose combined data enable studies of both cloud microphysics

147 and surface mass balance (Gorodetskaya et al. 2015). The British Antarctic Survey's Rothera
148 Station, in the southern Antarctic Peninsula region, serves as a base for aircraft-based in situ
149 cloud microphysical observations that have revealed details about warm-temperature secondary
150 ice production in Antarctic clouds (Lachlan-Cope et al. 2016). West Antarctica, due to its
151 extreme remoteness, has yet to see a permanent installation of atmospheric or climate science
152 instrumentation beyond AWS (Lazzara et al. 2012), but the AWARE campaign has made a start.
153 Figure 1 shows the location of the two AWARE deployments. Within the entire sector of
154 Antarctica shown in this figure, only four locations (indicated by red markers) have seen
155 atmospheric and climate science experiments using modern instrumentation with multiple
156 sensors: McMurdo Station and its immediate surroundings on and near the western Ross Ice
157 Shelf (RIS), South Pole Station, WAIS Divide Ice Camp, and Rothera Station.

158 This report on the AWARE campaign is organized with three scientific motivations. The
159 first is to illustrate contrasts between the Antarctic and the relatively better-observed Arctic. The
160 high Arctic is a partially frozen ocean surrounded by continental land masses, with one major ice
161 sheet (Greenland) contributing to sea level rise. The Arctic radiation budget is strongly
162 influenced by persistent and long-lived mixed-phase clouds (e.g., Morrison et al. 2011; Bennartz
163 et al. 2013). High southern latitudes are characterized by a continent with greatly varying
164 topography at high elevations surrounded by the world's most turbulent ocean. The SEB at the
165 vulnerable extremities of Antarctic ice sheets is influenced on one hand by katabatic and
166 topographic influences on atmospheric dynamics and cloud physics, and on the other hand by
167 adjacent Southern Ocean storm tracks (Nicolas and Bromwich 2011) that are in turn influenced
168 by teleconnections with lower latitudes. The more varied influences on Antarctic clouds often

169 yield markedly different manifestations of mixed-phase cloud microphysics than seen in the
170 Arctic (Scott and Lubin 2016).

171 A second motivation is the need to keep aerosol chemistry and microphysics on an equal
172 footing with meteorology and cloud microphysics. The study of aerosol-cloud interaction has
173 become inseparable from any thorough and current study of mixed-phase cloud lifecycle, and our
174 presentation of contrasts between the Antarctic and the Arctic must necessarily include aerosol
175 climatology. Finally, we demonstrate how AWARE data from West Antarctica can be used to
176 evaluate performance of both regional and climate models, in the region where atmospheric
177 warming is expected to exacerbate ice shelf loss and Antarctic contribution to sea level rise.

178

179 **Experiment Design**

180 AWARE deployed the second ARM Mobile Facility (AMF) to McMurdo Station on Ross
181 Island, Antarctica to sample an annual cycle in atmospheric structure and thermodynamics, surface
182 radiation budget and cloud properties. The ARM Mobile Facility deployments began in 2005 in
183 response to the substantial success that the three fixed ARM sites realized for gathering advanced
184 atmospheric sensor data for climate model development and validation (Mather and Voyles 2013).
185 The AMFs consist of cloud research radars, lidars, multiple broadband and spectral radiometers,
186 an aerosol observation suite, and thorough meteorological sampling ranging from surface turbulent
187 flux equipment to radiosondes. The AMFs are intended to address key issues in atmospheric
188 science by deploying the entire multi-sensor suite to a given location for at least several months of
189 data collection, thereby making a substantial advance in the field.

190 In October 2013 the AWARE campaign, organized by researchers from the Scripps
191 Institution of Oceanography (SIO), Byrd Polar and Climate Research Center (BPCRC),

192 Pennsylvania State University, and Brookhaven National Laboratory (BNL), was awarded the use
193 of the second Mobile Facility (AMF2) to address the current concerns related to Antarctic climatic
194 warming discussed above. Transportation, construction and power requirements of an AMF
195 necessitated the choice of McMurdo Station as the site for the full AMF deployment. At the same
196 time, the ARM program recognized the value in collecting data directly from West Antarctica, and
197 the AWARE campaign was fortunate to be awarded a second and smaller suite of instruments
198 optimized for SEB measurement for deployment at one of the summer-only field stations in West
199 Antarctica.

200 McMurdo Station (77°S50'47"S, 166°40'06"E) is generally a challenging location for
201 meteorological and aerosol sampling because of complex terrain variability and related
202 microclimates including rapidly shifting wind direction. The CosRay location 1 km from
203 McMurdo (Figure 2) provided the research radars with a clear view across an open fetch of water
204 in southeasterly through southwesterly directions, which are the prevailing wind directions. The
205 WAIS Divide Ice Camp (WAIS Divide; 79°28'03"S, 112°05'11"W, elevation 1797 m) was chosen
206 as the most logistically suitable station for the SEB measurement suite, based on power and
207 transportation constraints. The US Antarctic Program (USAP) allocated the AWARE campaign's
208 extended facility component (Figure 1) one LC-130 aircraft mission to transport to WAIS Divide
209 all personnel and equipment, including laboratory housing (half-size sea container) and helium for
210 radiosondes. The extremely flat and even terrain at WAIS Divide offered an ideal site for
211 radiometry and SEB measurement, with the largest instrumental challenge being optical
212 obstruction and occasional instrument fouling during extended periods of strong winds and
213 blowing snow. Figure 3 shows the sea container installation at WAIS Divide. Table 1 lists the
214 AMF2 instruments at CosRay and Table 2 lists the instruments deployed to WAIS Divide. These

215 tables also provide the instrument acronyms used in the text. At McMurdo Station the AMF2 began
216 full operation on 1 December 2015, with some instruments operating earlier, and continued
217 through 31 December 2016. At WAIS Divide, the AWARE instruments began operation with
218 sondes on 4 December 2015, with all instruments operating by 7 December and continuing until
219 17 January 2016.

220 In the following sections we demonstrate how climatological information on cloud
221 properties is derived from the AMF2 measurements, and we discuss contrasts with cloud properties
222 obtained from Arctic locations with nearly identical instrumentation. We also discuss AMF2 case
223 studies suitable for model evaluation, again contrasting AWARE retrievals from their Arctic
224 counterparts. We then illustrate how the WAIS Divide dataset can be used as a case study for both
225 regional and global climate model evaluation regarding cloud microphysics. At WAIS Divide
226 AWARE was fortunate to sample the edge of a surface melt event that spanned a third of West
227 Antarctica and most of the Ross Ice Shelf (RIS) and lasted from 10 to 18 January 2016 at WAIS
228 Divide (Nicolas et al. 2017). The rapid transition between climatologically typical summer
229 conditions and the much warmer conditions of the melt onset represents a step function that
230 provides a stringent test of microphysical parameterization performance in response to the
231 changing model input fields (e.g., Wilson et al. 2018).

232

233 **Preliminary Instrumental Results and Arctic Comparison**

234 *Climatological Comparisons*

235 Silber et al. (2018a,b; 2019a) have developed a multi-sensor approach to determine key
236 climatological cloud properties from high latitude ARM data, including occurrence fraction, cloud
237 persistence and boundaries, and cloud location relative to temperature and moisture inversions. In

238 the application of this approach at McMurdo, Ka-band ARM zenith radar (KAZR) data from both
239 general and moderate sensitivity operating modes are used for hydrometeor detection throughout
240 the troposphere, similar to Clothiaux et al. (2001), and these detections are gridded to the High
241 Spectral Resolution Lidar (HSRL) 7.5 meter vertical resolution and 30-second time sampling.
242 HSRL data are then used to refine the cloud detection process by analyzing the log-scaled
243 particulate backscatter cross section β_p as a function of the linear depolarization ratio (LDR).
244 Different regions in the scatter diagram of β_p versus LDR correspond to liquid water droplets,
245 cloud ice particles, or aerosol particles, and the observational occurrence in each of these regions
246 provides climatological information as a function of altitude.

247 The multi-sensor approach used here is optimized for polar regions. The liquid water cloud
248 base height algorithm in Silber et al. (2018b) differs from earlier ARM retrievals in that it is
249 optimized for detection of a polar cloud base, as opposed to any cloud base (e.g., as in ceilometer
250 algorithms). This algorithm uses the backscatter cross section's first and second derivatives to
251 accurately determine the cloud base height. The hydrometeor detection algorithm described in
252 Silber et al. (2018a; 2019a) using lidar is based on identifying local minima in monthly histograms
253 of backscatter versus LDR, such that no fixed backscatter and/or LDR thresholds for liquid or ice
254 are used, but instead, adaptive dependent thresholds may vary in time, thereby reducing error in
255 phase classification. Hydrometeor detection using KAZR as describe in Silber et al. (2018a) is
256 based on a signal-to-noise ratio (SNR) threshold but is otherwise not significantly different than
257 earlier ARM retrieval methods.

258 This multi-sensor approach is applied here to both McMurdo AMF2 and ARM North Slope
259 of Alaska (NSA) data, with climatological contrasts demonstrated in Figures 4-7. The NSA site is
260 located at Utqiagvik (71.3°N, 156.8°W, formerly referred to as Barrow, Alaska), adjacent to the

261 Beaufort Sea, and is representative of an Arctic maritime location with variable sea ice
262 concentration. Instrumentation at the NSA site is very similar to the AMF2 deployed at McMurdo,
263 and the ARM data reduction and quality control pipeline is identical for the two sites (Peppler et
264 al. 2008). The NSA data analysis presented here is based on measurements from 2015, which
265 correspond with previous analyses of longer datasets from this site (e.g., Shupe 2011).

266 Figure 4 shows thirty-day running-mean total hydrometeor and liquid-cloud occurrence
267 fractions at McMurdo and NSA over an annual cycle. The total duration is 721 hours, and an odd
268 hour number was required for the smoothing to center the data properly, hence the indication of
269 plus one hour in the caption. The temperature curve, based on radiosonde profiles, represents the
270 average temperature between the surface and 4 km altitude. We see that the annual hydrometeor
271 (liquid) occurrence fraction is higher by ~20% (~31%) at NSA relative to McMurdo. Figure 5
272 shows seasonal averages of cloud thickness, highest cloud top height and highest cloud top
273 temperature. Here the highest cloud top height is the highest bin with any detected hydrometeor
274 using the combined HSRL and KAZR method of Silber et al. (2018b), and the highest cloud top
275 temperature is the corresponding temperature computed from the sonde data linearly interpolated
276 in time. Most clouds are thicker at McMurdo relative to NSA, but the deepest, likely frontal, clouds
277 are observed at NSA. The annual highest cloud-top heights are more variable at NSA but generally
278 comparable at both sites (both having elevation close to sea level), while the highest cloud-top
279 temperatures are mostly lower and less variable at McMurdo.

280 Figure 6 provides similar seasonal averages of total cloud and liquid-bearing layer
281 persistence. Liquid-cloud layers are significantly more persistent at NSA than McMurdo, a result
282 likely influenced by (1) the complex topography and lack of significant moisture sources at
283 McMurdo relative to NSA (Monaghan et al. 2005), and (2) synoptic flow and advection being

284 different for the two sites. While the longest-lived layers are observed in summer at NSA,
285 McMurdo exhibits different seasonal behavior (depending on the examined percentile). Figure 7
286 illustrates the seasonal variability of the lowest liquid-bearing cloud layer base height, as well as
287 its annual cumulative distribution function. The lowest liquid-bearing cloud layers are significantly
288 higher at McMurdo relative to NSA, but liquid is detected at higher altitudes at NSA, due to
289 typically warmer temperatures in the atmospheric profile (Figure 5). These cloud layers are evenly
290 distributed up to ~3 km at McMurdo while over NSA, they are mostly concentrated near the
291 surface.

292 Statistical significance of the comparisons between McMurdo and Utqiagvik in Figures 4-
293 7 was assessed using a two-sample Kolmogorov-Smirnov test at the 95% confidence level, to
294 determine if the samples represent different variable distributions. The distributions were found to
295 be different at this confidence level for all retrievals in Figures 4, 5 and 7, and for liquid water
296 clouds during spring in Figure 6.

297 The distribution of aerosol particles in the Antarctic is characterized by its unique location
298 and surrounding ocean (which largely isolates it from the sources present on other continents), its
299 near-complete coverage by ice and snow (which eliminates most local non-sea-salt-dust and
300 terrestrial biological particle sources), and its near-absence of human activities (which minimizes
301 the emissions from combustion, cooking, and other human activities). The lack of orographic
302 features in the Southern Ocean surrounding Antarctica supports the midlatitude westerlies,
303 effectively defying substantial transport of continental emissions into the Antarctic region. The
304 result is that aerosol concentrations reflect the seasonal trends of ocean phytoplankton (non-sea-
305 salt-sulfate), seabirds (organic mass), wind-driven sea spray (salt), and non-sea-salt-dust, as is
306 shown in Figure 8 (Panel B).

307 The OM concentration is highest in summer during AWARE, when seabird activity is also
308 high. The breakdown products of urea deposits from seabirds result in a variety of organic
309 products in the vapor phase (Legrand et al. 2012), some of which condense and, along with
310 ammonia (Legrand et al. 1998), contribute to particle-phase ammonium and OM. Of course human
311 activities at McMurdo Station, while minimal compared to those of urban regions, also contribute
312 OM, but in the summer that accounts for less than half of the observed OM (Figure 3 of Liu et al.
313 [2018]). Some OM may also be associated with the submicron salt from sea spray, but the Fourier-
314 transform infrared spectroscopy (FTIR) spectra are more consistent with seabird sources (Schmale
315 et al. 2013) and the seasonal trend of OM concentration is not consistent with an association with
316 salt from sea spray (Liu et al. 2018). Even though the non-sea-salt-sulfate concentration tracks the
317 OM closely, the strong summertime signature is likely attributable nearly entirely to a different
318 source, namely the production of DMS by ocean phytoplankton and subsequent oxidation to form
319 non-sea-salt-sulfate. Submicron non-sea-salt-dust mass concentration is also highest in summer,
320 likely as a result of both increased human activities and more exposed soil. During AWARE, the
321 salt mass concentration is very small, with seasonal means and medians from 0.02 to 0.11 $\mu\text{g m}^{-3}$
322 and maximum weekly values below 0.2 $\mu\text{g m}^{-3}$ in winter. This cycle is driven by the local upwind
323 wind speeds at the sea surface as well as the additional contributions of wind-driven frost flowers
324 on new sea ice in winter (Liu et al. 2018).

325 In Figure 9 we present data from two Arctic sites for comparison with AWARE. Figure 10
326 provides seasonal statistics comparing Utqiagvik with AWARE. At the Alert Observatory
327 (82.45°N, 62.51°W; Leitch et al. 2018), the contributions from organic functional groups to the
328 Arctic submicron aerosol were measured using 126 weekly-integrated samples collected from
329 April 2012 to October 2014. Routine outdoor high-volume samples of total suspended particles

330 have been collected at Alert for inorganic chemical composition since 1980 (e.g., Barrie and Hoff,
331 1985), and submicron sampling for inorganic ion analysis was started in March 2011. As a special
332 study, weekly collections of particles smaller than 1 μm on Teflon filters were collected for Fourier
333 transform infrared (FTIR) spectroscopy of organic functional groups (OFG) from April 2012 to
334 October 2014.

335 At Alert the cycle in salt mass concentration is similar to that of AWARE, with as much
336 as $0.5 \mu\text{g m}^{-3}$ in winter and below $0.1 \mu\text{g m}^{-3}$ in summer (Figure 9). At NSA the winter
337 concentrations are higher with a mean of 1 and weekly-averaged values of up to $2 \mu\text{g m}^{-3}$,
338 consistent with the closer proximity to seasonal new sea ice associated with higher frost flower
339 frequency (Shaw et al. 2010; Xu et al. 2013, 2016). The evidence for Na depletion relative to Cl
340 supports a wintertime contribution from frost flowers during AWARE (Liu et al. 2018), since the
341 higher freezing temperature of Na salts relative to Cl salts indicates the role of wicking from brine
342 pools in particle formation.

343 In contrast, the highest non-sea-salt-sulfate and organic mass concentrations in the annual
344 cycles in the Arctic at both NSA and Alert show the well-known springtime haze that results from
345 transport from the northern mid-latitudes, as illustrated in Figure 9 (Shaw 1982; Law and Stohl
346 2007; Quinn et al. 2007). The overall low concentrations of submicron mass concentration are
347 otherwise a common feature of the Arctic and Antarctic. The Utqiagvik sulfate mass
348 concentration means and medians in winter and spring exceed those of summer and autumn by
349 more than a factor of two, obscuring any smaller differences that could be present for biological
350 sources of non-sea-salt-sulfate between summer and winter seasons. Another interesting difference
351 is the relative amount of non-sea-salt-sulfate to organic mass, which is nearly 1:1 in summer at
352 AWARE and NSA, but it exceeds 2:1 at Alert, especially in early spring. Summer sulphate (and

353 OM) at Alert, after June, is primarily biological with some transient contributions from biomass
354 burning (BB). Utqiagvik is likely similar, but has a larger contribution to OM from BB during the
355 summer, giving the smaller SO₄/OM value. In spring (and winter), both sites experience transport
356 from Eurasia with Utqiagvik seeing a little more from SE Asia (e.g., Xu et al. 2017). OM relative
357 to sulphate is similar at both sites.

358 The higher organic and non-sea-salt-sulfate mass concentration in summer in Antarctica is
359 coincident with higher concentrations of CCN at supersaturations of 0.1% and 1% (Panel A of
360 Figure 8). This correlation means that the biogenic non-sea-salt-sulfate and organic sources may
361 well both contribute significantly to summertime CCN concentrations, as they do in the Arctic
362 (Abbatt et al. 2019). The relationship between biogenic non-sea-salt-sulfate and organic means
363 that both can have an effect on cloud droplet number concentrations, potentially increasing cloud
364 drop effective radius and shortwave reflection.

365 *Examples of Representative Individual Cases*

366 Following these climatological comparisons, we now discuss some representative
367 individual cases that illustrate the potential for evaluating climate model simulations with nearly
368 identical multi-sensor data sets from both the Antarctic and the Arctic. AWARE obtained the first
369 ever triple-wavelength radar observations of ice and mixed-phase clouds over Antarctica. These
370 observations point to a new paradigm in unraveling ice microphysics processes at high latitudes.
371 When observing ice particles with a single-wavelength radar in the “Rayleigh regime” (i.e., when
372 the wavelength is large compared to the size of the ice particles), the radar reflectivity Z is
373 proportional to the square of the particle masses $m(D)$ integrated over the particle size distribution
374 (PSD) but it is more intricately related to other moments of the PSD, for example the cloud ice
375 water content (IWC) or the ice mass flux, which are indeed the most relevant for microphysical

376 studies. When the wavelength of the radars becomes comparable to the size of the particles being
377 probed (“non-Rayleigh” regime) the measured reflectivity decreases sometimes by more than 10
378 dB relative to the Rayleigh reference (Matrosov 1998; Kneifel et al. 2011; 2015). The main reason
379 for this decrease is that interferences (usually destructive) of the incident wave and reflected waves
380 from different parts of the particle cause the backscattered energy to be smaller than for pure
381 Rayleigh scatterers.

382 Dual-wavelength reflectivity ratios (DWR) are then indicative of a characteristic size of
383 the PSD such as mass median diameter (Matrosov 1998; Kneifel et al 2011). Depending on the
384 radar wavelength pair, they are particularly effective within specific particle size ranges. For
385 example, the Ka-W frequency pair is effective for a particle size range between 0.5 and 3 mm,
386 whereas to cause a difference at X-Ka frequencies the particle size has to exceed sizes of ~8 mm.
387 When more than two frequencies are considered not only can the characteristic size of the ice PSD
388 be derived for broader size ranges but also information on bulk density can be gleaned (Kulie et
389 al. 2014; Leinonen and Moisseev 2015; Kneifel et al. 2015; Stein et al. 2015), which better
390 constrains the ice microphysics.

391 Figure 11 shows a two-dimensional histogram of the data collected at McMurdo during 10
392 January 2016 from the X-Ka- and W-band ARM radars. While most of the data are concentrated
393 around the origin (0dB, 0dB), thereby corresponding to small ice crystals that produce the same
394 reflectivities at all frequencies, histogram bins with large DWRs signal the presence of larger ice
395 crystals. Following the rationale proposed by Kneifel et al. (2015) the three different branches
396 indicated by the continuous, dotted and dashed lines correspond to different growth mechanisms.
397 For example, the typical hook signature (continuous line) is likely associated with low-density
398 aggregates, while the points with large Ka-W and small X-Ka DWR (dashed line) are linked to

399 denser and more spherical particles. Retrieval methodologies focused at using this information in
400 a quantitative way are currently under study (Leinonen et al. 2018; Chase et al., 2018; Mason et
401 al., 2018; Battaglia et al. 2019). Surprisingly, the strength of the observed multi-frequency radar
402 signatures are overall in a similar range (both DWRs exceeding 10 dB) as observed during the
403 deployment of the AMF2 at the Biogenic Aerosols-Effects on Clouds and Climate (BAECC, Petäjä
404 et al., 2016) campaign in Finland (Kneifel et al., 2015). The unexpected strong multi-frequency
405 radar signatures revealed during AWARE indicate that growth processes such as aggregation and
406 riming play an important role in the processes related to snowfall production in Antarctica – at
407 least in areas with sufficient supply of moisture such as close to the coast.

408 ARM’s extensive multi-spectral capabilities deployed at McMurdo Station offer the ability
409 to construct specific case studies for model evaluation (e.g., Silber et al., 2019b), as has been done
410 with several Arctic field campaigns (e.g., Fridlind et al. 2007; Verlinde et al. 2007; McFarquhar et
411 al. 2011; Fridlind and Ackerman 2018). Here we demonstrate some AWARE ground-based remote
412 sensing retrievals and contrasting Arctic cases from NSA. Figure 12 shows two representative
413 examples of mixed-phase clouds observed at McMurdo and at the ARM NSA Utqiagvik site as
414 detected by the HSRL at visible wavelengths (532 nm) and the KAZR at millimeter wavelengths
415 (~8.5 mm). As the two instruments operate at wavelengths that differ by four orders of magnitude,
416 their measurements are sensitive to different aspects of the cloud. The lidar is more sensitive than
417 radar to small particles with high number concentrations such as liquid droplets, as seen at the top
418 of the cloud by a region of strong backscatter (Figure 12 a,b) and a low depolarization ratio
419 indicating spherical droplets (Figure 12 c,d). Ice particles form in the layer of supercooled liquid
420 water that precipitate from its base. This is seen as significantly nonzero lidar depolarization ratios
421 indicating nonspherical particles (Figure 12 c,d) that are large enough to strongly reflect energy at

422 the significantly longer radar wavelengths (Figure 12 e,f). The mixed-phase clouds shown are
423 representative in that the clouds at Utqiagvik tend to form in the boundary layer with the ice virga
424 often reaching the surface, while the McMurdo clouds tend to form above the boundary layer; the
425 latter probably being related to the strong katabatic flow and other topographic effects (see Figure
426 7; see also Silber et al., 2018a; Zhang et al. 2019).

427 Retrievals from the Atmospheric Emitted Radiance Interferometer (AERI) provide an
428 important complement to the HSRL and radar measurements. The magnitude and spectral shape
429 of the downwelling longwave radiance measured by the AERI from 8 to 25 μm is sensitive to
430 cloud temperature, optical depth, thermodynamic phase and particle effective radius. Cloud
431 properties retrieved from AERI measurements using the Cloud and Atmospheric Radiation
432 Retrieval Algorithm (CLARRA; Rowe et al. 2019) are shown in Figure 11(g-n).

433 The full year of measurements at McMurdo allows comparison of Arctic and Antarctic
434 clouds over a full seasonal cycle. As an example, Figure 12 compares Arctic and Antarctic clouds
435 for two time periods. The dates were chosen such that temperatures are similar at the cloud heights
436 (-30° to -20°C) and where supercooled cloud liquid water can exist. Although surface temperatures
437 differed markedly for these two cases, four other cases were also considered for which surface
438 temperatures were similar between locations (08 March 2016 and 13 March 2016 at McMurdo,
439 and 05 November 2014 and 20 January 2016 at Utqiagvik; not shown). For all cases, the optical
440 depth of liquid is higher than for ice (Figures 12 g and h) and variations in optical depth, liquid
441 effective radius and liquid water path are typically correlated with each other. However,
442 differences are apparent in clouds between the two locations. At McMurdo clouds are higher
443 (Figure 12 a-f) and optically thinner overall (Figure 12 g, h), and liquid droplets typically have
444 smaller effective radii (Figure 12 i, j) for these cases. Similar contrasts were also found between

445 the two locations for the other case examined. For example, the liquid effective radii at Utqiagvik
446 was found to be typically between 4 and 10 μm , in keeping with previous measurements in the
447 Arctic (e.g., Cox et al. 2014), whereas at McMurdo it was typically below 5 μm . The latter is
448 consistent with Zhang et al. (2019), who find similar small values for McMurdo using active-
449 sensor techniques described in Snider et al. (2017). Work is in progress to retrieve and compare
450 cloud microphysical properties including liquid and ice optical depths and effective particle sizes
451 over a full year.

452

453 **Climate Modeling Applications**

454 The AWARE campaign's first major result came from WAIS Divide, when the sea
455 container equipment recorded atmospheric and SEB fluxes at the edge of a major West Antarctic
456 melt event (Nicolas et al. 2017). This melt event was associated with a strong El Niño year. The
457 onset of the melt event on 10 January was accompanied by an abrupt temperature increase at WAIS
458 Divide (Figure 13). The immediate cause of this melt event was an amplified high-pressure ridge
459 ("blocking high") over the 90–120°W sector of the Southern Ocean. By creating a prominent dent
460 in the circumpolar westerly flow, this ridge generated a strong north-south advection of warm
461 marine air toward West Antarctica. The ridge was strongest during 10–13 January 2016 but
462 persisted through 20 January, maintaining warm conditions favorable to surface melt in the sector
463 West Antarctica adjacent to the RIS. Positive sea surface temperature anomalies of $>2^{\circ}\text{C}$ near
464 50°S, 120°W provided additional heat to the air traveling south. The unusual extent and duration
465 make the melt event one of the greatest observed in the RIS since the beginning of the satellite
466 record in 1978 (Nicolas et al. 2017). The SEB evolution was derived from nearly all the AWARE
467 instruments at WAIS Divide and is described in Nicolas et al. (2017). The "step function" in

468 temperature and moisture throughout the lower troposphere that occurred around 10 January,
469 captured by AWARE instruments, provides a unique case study for both regional and global
470 climate models.

471 In Figure 13 we show an evaluation of the Polar Weather Research and Forecasting
472 regional model (PWRF), which is a version of the Weather Research and Forecasting (WRF)
473 model (Skamarock et al. 2008) adapted for high latitudes (e.g., Hines and Bromwich 2017); this
474 comparison complements the comprehensive investigation by Hines et al. (2019) of the WAIS
475 Divide warming using PWRF simulations. Here Polar WRF uses a double-moment cloud
476 microphysics scheme (Morrison et al. 2005), and is initialized in the first simulation using ERA-
477 Interim (PWRF-EI; Dee et al. 2011) and then in the second using analysis data from the NOAA
478 Global Forecast System (GFS; PWRF-FNL). Figure 12 focuses on the transition period 8-13
479 January 2016 when the step function in tropospheric temperature and moisture occurred. We first
480 consider the precipitable water vapor (PWV), comparing both simulations against observations
481 from the AWARE MWR retrievals. These WAIS Divide radiosonde data, used to derive the MWR
482 PWV retrievals, were not contributed to the Global Telecommunication System (GTS) that feeds
483 information into data assimilation for global meteorological reanalyses; and therefore we have an
484 independent assessment of model performance at a completely data-sparse location. Both
485 simulations capture much of the observed time evolution of this field, but there are key differences
486 late on 10 January and throughout 11-12 January.

487 The PWV from the analysis/reanalysis should have a strong impact on the produced cloud
488 liquid water in mesoscale simulations, and this is seen in the time evolution of cloud liquid water
489 path (LWP). Observations show relatively high occurrence of liquid water on 9-10 January, and
490 the simulations failed to capture this. The analyzed water vapor field may contribute to the error.

491 The ERA-Interim simulation does a better job of capturing the liquid water early on the 11 January.
492 Later in the day, more liquid water is simulated than observed. Liquid water is generally under-
493 simulated on 12 January.

494 The third panel in Figure 13 shows the 2-m air temperature. The near-surface temperature
495 should be important for tracking West Antarctic melting. Early on 10 January, little cloud liquid
496 water is simulated, and as a possible result the simulations are several degrees too cold. However,
497 much of the warming event during the latter half of 10 January is captured by the simulations
498 (compare top and bottom panels). The simulation driven by ERA-Interim better captures the liquid
499 water during the first half of the 11 January, so it better represents the temperature.

500 Figure 14 illustrates a global climate model (GCM) evaluation example, for GCMs
501 presently under development, again using the WAIS Divide melt event data as a case study. The
502 models considered here are the first version of the atmospheric component of the DOE Energy
503 Exascale Earth System Model (E3SM), EAMv1 (see Rasch et al. 2019), and the most recent update
504 of the NASA Goddard Institute for Space Studies (GISS) GCM (Schmidt et al. 2014), the ModelE.
505 Fields used to nudge horizontal winds in ModI3 and run EAMv1 are taken from ERA5, the fifth-
506 generation atmospheric reanalysis from the European Centre for Medium-Range Weather
507 Forecasts (ECMWF) (Hersbach and Dee 2016). Results show that both models generally simulate
508 the PWV well (Figure 14a), but that both models overestimate the LWP of the supercooled clouds,
509 particularly for E3SMv1 (Figure 14b). These overestimations have important consequences to the
510 amount of energy into the snowpack (netSnowpack) at the WAIS Divide, computed as the residual
511 of the net shortwave and longwave radiative energy (netRadiation) into the surface minus the
512 turbulent fluxes (sensible and latent heating) removing energy from the surface (netTurbulence):

513 (1) $\text{netSnowpack} = \text{netRadiation} - \text{netTurbulence}$

514 An interesting interplay is seen among these terms in Figure 14c-e. The netRadiation term for both
515 models tends to have a positive bias (too much energy into the snowpack), although ModelE has
516 a greater day-to-day oscillation about zero net flux than does EAMv1 (Figure 14c). The turbulent
517 flux of energy away from the snowpack's surface, netTurbulence, is positively biased for EAMv1
518 while ModelE generally performs well (Figure 14d). The net effect of the radiative and turbulent
519 fluxes on the energy into the snowpack (Figure 14e) shows that the positive biases for EAMv1
520 largely cancel, while the oscillatory nature of the radiative component for ModelE tends to
521 dominate its good simulation of the surface turbulence. A likely contributor to the radiative biases
522 for both models is the change in the surface longwave radiative flux resulting from errors in the
523 LWP that affect cloud emissivity (e.g., Silber et al. 2019c). Figure 14f shows the model bias
524 relative to observations of the net longwave radiation at the surface versus the LWP bias. The plot
525 shows a clear tendency for overestimates in LWP to yield overestimates in surface longwave flux,
526 and vice versa, indicating that the LWP bias is an important factor. Collectively, the results in this
527 figure demonstrate the ability to attribute model biases using component analyses made available
528 from the AWARE data.

529

530 **Summary and Future Work**

531 Any time-limited field campaign, even one such as AWARE with its robust suite of
532 instruments and relatively longer duration (one year), has associated issues regarding
533 representativeness. Geographically, the AMF2 deployment at McMurdo sampled an Antarctic
534 coastal location with adjacent high terrain with complex topography, such that cloud formation
535 and persistence are often influenced by katabatic flows and/or terrain-induced gravity waves. This
536 general situation might apply to numerous coastal Antarctic locations. The AWARE

537 instrumentation at WAIS Divide sampled the SEB under cloud cover representative of most of
538 West Antarctica (e.g., Scott et al. 2017), although WAIS Divide is at a much higher elevation than
539 the West Antarctic ice shelves that are most vulnerable to a warming climate. Hence the SEB
540 measurements during the January 2016 melt event describe a precursor to and onset of surface
541 melt, rather than a fully developed surface melt that directly impacts an ice shelf or ice cliff via
542 hydrofracturing. AWARE did not make any measurements on the high terrain of East Antarctica,
543 and so a researcher should be very careful about generalizing AWARE findings in cloud physics
544 or aerosol microphysics and chemistry to East Antarctica. Regarding climatology of the specific
545 regions sampled, AWARE trailed a large ENSO event and was then followed by unprecedented
546 sea ice loss and another extensive surface melt event the following spring linked to strong negative
547 Southern Annular Mode (SAM) index combined with a positive index in the first Pacific-South
548 America pattern having a classic Rossby wave-train structure (Scott et al. 2019). AWARE data
549 from both McMurdo Station and WAIS Divide might therefore be representative of warmer than
550 normal conditions compared with recent climatology.

551 Although separated by 1600 km, there is often a meteorological relationship between the
552 two AWARE sites at McMurdo Station and WAIS Divide Ice Camp. Low-pressure troughs in the
553 Ross Sea frequently bring moisture and cloud cover over the WAIS, which can eventually descend
554 onto the Ross Ice Shelf and reach Ross Island from a southerly direction (Coggins et al. 2014;
555 Nicro and Cassano 2014; Silber et al., 2019a). This is particularly evident in case studies described
556 in Scott and Lubin (2014). In contrast to the Arctic, this air mass trajectory also traverses mountain
557 ranges that cause substantial orographic lifting and related ice cloud formation (Scott and Lubin
558 2016). Tracking of these synoptic-scale patterns by satellite remote sensing and validation of the

559 “end point” in cloud evolution from AWARE measurements at McMurdo might provide further
560 insight into mixed-phase cloud properties that are distinct from the Arctic.

561 In the first Antarctic climatological assessment from AWARE data presented here, we have
562 seen many contrasts with the high Arctic. These include persistent differences in liquid cloud
563 occurrence, cloud height and cloud thickness. Antarctic aerosol properties are also quite different
564 from the Arctic, due to the continent’s isolation from lower latitudes by Southern Ocean storm
565 tracks. This brings a seasonal cycle in which most aerosol constituents have maximum
566 concentration in summer, and in which abundances are almost entirely from a variety of Antarctic
567 rather than transported sources. Comparable measurements from two high Arctic sites show
568 springtime maxima comprising the “Arctic haze” that has origins from northern mid-latitudes.
569 AWARE data show that Antarctic aerosol abundances are not negligible despite the large-scale
570 dynamical isolation, and the aerosol chemical composition revealed by AWARE measurements
571 implies that aerosol-cloud interaction in the Antarctic deserves further study.

572 In the preliminary model evaluations presented here, we have considered the WAIS Divide
573 case study sufficiently to note some basic discrepancies between simulations and observations.
574 Much work needs to be done on the specific cloud microphysical parameterizations, or other model
575 components, to realize improvements to model performance over Antarctica. The AMF2 data are
576 an additional resource for developing very stringent tests of mixed-phase cloud parameterization
577 performance. In addition to the orographic forcing by the Transantarctic Mountains that causes
578 climatological contrasts from the Arctic, terrain variability in the local Ross Island area often
579 induces low-level gravity waves that produce unique mixed-phase cloud realizations. The
580 AWARE science team is presently constructing some AMF2 case studies that might be suitable
581 for model evaluation and improvement, and many coauthors on this paper already have experience

582 with AWARE data that could assist other researchers with selecting data for a variety of modeling
583 requirements. Finally, AWARE data should be valuable for planning future Antarctic fieldwork
584 using advanced instrumentation. Examination of the AWARE campaign data in the online ARM
585 Archive can provide guidance for what to expect when various types of meteorological and remote
586 sensing equipment are deployed for extended Antarctic research programs.

587

588 **Acknowledgements**

589 AWARE was jointly sponsored and supported by the US Department of Energy
590 Atmospheric Radiation Measurement (ARM) Program and the National Science Foundation via
591 the United States Antarctic Program. AWARE data are available online at the ARM data archive.
592 DL, DHB, KH, IS, JV and LMR were supported by US Department of Energy Grant DE-
593 SC0017981 and NSF Grant PLR-1443549. DZ and AMV were supported by the US Department
594 of Energy under Grant DE-SC0012704. RCS was supported by NASA Earth & Space Science
595 Fellowship grant NNX15AN45H. AB and SK were supported by US Department of Energy Grant
596 DE-SC0017967, with additional support for SK by the German Research Foundation (DFG) via
597 the Emmy-Noether Program (Grant KN 1112/2-1). MC is supported by the US Department of
598 Energy under contract DE-AC02-06CH11357. PR was supported by NSF Grant PLR-1543236.
599 AMF was supported by the NASA Radiation Science Program and Modeling, Analysis and
600 Prediction Program. Resources supporting this work were provided by the NASA High-End
601 Computing (HEC) Program through the NASA Center for Climate Simulation (NCCS) at Goddard
602 Space Flight Center. AMF and IS thank Andrew Ackerman and Maxwell Kelley for their
603 assistance using ModleE3. Utqiagvik aerosol measurements were supported by NSF Grant ARC-
604 0714052 and Alert aerosol measurements were supported by the Grants and Contributions program

605 of ECCC. The authors are thankful to the technicians, operators, and students who assisted with
606 the aerosol measurements reported here, and in particular Patrick Shaw, Anne Jefferson, and Lelia
607 Hawkins for Utqiagvik, Desiree Toom and the Department of Defense Canadian Forces staff at
608 Alert, and Jun Liu for the FTIR and XRF analysis for AWARE
609 (<https://doi.org/10.6075/J0WM1BKV>). Retrievals from the AERI instrument use CO₂
610 concentrations from CarbonTracker (version CT2017, NOAA ESRL;
611 <http://carbontracker.noaa.gov>; Peters et al. 2007), ozone, temperature, and pressure data from
612 ERA-interim. This paper is PMEL contribution number 4976. This paper is contribution number
613 1587 of the Byrd Polar and Climate Research Center.

614

615 **References**

- 616 Abbatt, J. P. D., and Coauthors, 2019: Overview paper: New insights into aerosol and climate in
617 the Arctic, *Atmos. Chem. Phys.*, **19**, 2527-2560, <https://doi.org/10.5194/acp-19-2527-2019>.
- 618 Alley, R. B., S. Anandakrishnan, K. Christianson, H. J. Horgan, A. Muto, B. R. Parizek, D. Pollard,
619 and R. T. Walker, 2015: Oceanic forcing of ice-sheet retreat: West Antarctica and more.
620 *Annu. Rev. Earth. Planet. Sci.*, **43**, 207-31, doi:10.1146/annurev-earth-060614-105344.
- 621 Barrie, L. A., and R. M. Hoff, 1985: Five years of air chemistry observations in the Canadian Arctic.
622 *Atmos. Environ.*, **19**, 1995-2010, [https://doi.org/10.1016/0004-6981\(85\)90108-8](https://doi.org/10.1016/0004-6981(85)90108-8).
- 623 Bassis, J. N., and S. Jacobs, 2013: Diverse calving patterns linked to glacier geometry. *Nat.*
624 *Geosci.*, **6**, 834-836, doi:10.1038/NGEO1887.
- 625 Bates, T. S., and Coauthors, 2012: Measurements of ocean derived aerosol off the coast of
626 California. *J. Geophys. Res.*, **117**, D00V15, doi:10.1029/2012JD017588.

627 Battaglia, A., S. Tanelli, F. Tridon, S. Kneifel, J. Leinonen, and P. Kollias, 2019: Triple-frequency
628 radar retrievals. *Satellite Precipitation Measurement*, V. Levizzani, Ed., Springer,
629 submitted.

630 Bennartz, R., M. D. Shupe, D. D. Turner, V. P. Walden, K. Steffen, C. J. Cox, M. S. Kulie, N. B.
631 Miller, and C. Pettersen, 2013: July 2012 Greenland melt extent enhanced by low-level
632 liquid clouds. *Nature*, **496**, 83-86, doi:10.1038/nature12002.

633 Bromwich, D. H., J. P. Nicolas, K. M. Hines, J. E. Kay, E. L. Key, M. A. Lazzara, D. Lubin, G.
634 M. McFarquhar, I. Gorodetskaya, D. P. Grosvenor, T. Lachlan-Cope, and N. van Lipzig,
635 2012: Tropospheric clouds in Antarctica. *Rev. Geophys.*, **50**, RG1004.
636 doi:10.1029/2011RG000363.

637 Bromwich, D. H., J. P. Nicolas, A. J. Monaghan, M. A. Lazzara, L. M. Keller, G. A. Weidner,
638 and A. B. Wilson, 2013: Central West Antarctica among the most rapidly warming
639 regions on Earth. *Nat. Geosci.*, **6**, 139-145, doi:10.1038/NGEO1671.

640 Chase, R. J., J. A. Finlon, P. Borque, G. M. McFarquhar, S. W. Nesbitt, S. Tanelli, O. O. Sy, S.
641 L. Durden, and M. R. Poellot, 2018: Evaluation of triple-frequency radar retrieval of
642 snowfall properties using coincident airborne in situ observations during OLYMPEX.
643 *Geophys. Res. Lett.*, **45**, 5752–5760, doi:10.1029/2018GL077997.

644 Clothiaux, E. E., and Coauthors, 2011: The ARM Millimeter Wave Cloud Radars (MMCRs) and
645 the Active Remote Sensing of Clouds (ARSCL) Value Added Product (VAP). DOE
646 Tech. Memo. ARM VAP002.1, 55 pp.,
647 https://www.arm.gov/publications/tech_reports/arm-vap-002-1.pdf.

648 Coggins, J. A., A. J. McDonald, and B. Jolly, 2014: Synoptic climatology of the Ross Ice Shelf
649 and Ross Sea region of Antarctica: k-means clustering and validation. *Int. J. Climatol.*,
650 **34**, 2330-2348, <https://doi.org/10.1002/joc.3842>.

651 Cox, C. J., D. D. Turner, P. M. Rowe, and M. D. Shupe: 2014: Cloud microphysical properties
652 retrieved from downwelling infrared radiance measurements made at Eureka, Nunavut,
653 Canada (2006-09). *J. Appl. Meteorol. Clim.*, **53**, 772-791, doi:10.1175/JAMC-D-13-
654 0113.1.

655 Dee, D. P., and Coauthors, 2011: The ERA- Interim reanalysis: configuration and performance
656 of the data assimilation system. *Q. J. R. Meteorol. Soc.*, **137**, 553-597.
657 doi:10.1002/qj.828.

658 Ding, Q., E. J. Steig, D. S. Battisti, and M. Küttel., 2011: Winter warming in West Antarctica
659 caused by central tropical Pacific warming. *Nat. Geosci.*, **4**, 398-403,
660 doi:10.1038/ngeo1129.

661 Docquier, D., D. Pollard, and F. Pattyn, 2014: Thwaites Glacier grounding-line retreat: Influence
662 of width and buttressing parameterizations. *J. Glaciol.*, **60**, 305-313,
663 doi:10.3189/2014/JoG13J117.

664 Elvidge, A. D., I. A. Renfrew, J. C. King, A. Orr, T. A. Lachlan-Cope, M. Weeks, and S. L.
665 Gray, 2015: Foehn jets over the Larsen C Ice Shelf, Antarctica, *Quarterly Journal of the*
666 *Royal Meteorological Society*, **141**, 698-713, doi:10.1002/qj2382.

667 Fridlind, A. M., and A. S. Ackerman, 2018: Simulations of Arctic mixed-phase boundary layer
668 clouds: Advances in understanding and outstanding questions. *Mixed-Phase Clouds*, C.
669 Andronache, Ed., Elsevier, 153-183, [https://doi.org/10.1016/B978-0-12-810549-8.00007-](https://doi.org/10.1016/B978-0-12-810549-8.00007-6)
670 6.

671 Fridlind, A. M., A. S. Ackerman, G. McFarquhar, G. Zhang, M. R. Poellot, P. J. DeMott, A. J.
672 Prenni, and A. J. Heymsfield, 2007: Ice properties of single-layer stratocumulus during
673 the Mixed-Phase Arctic Cloud Experiment: 2. Model results. *J. Geophys. Res.*, **112**,
674 D24202, doi:10.1029/2007JD008646.

675 Frossard, A. A., P. M. Shaw, L. M. Russell, J. H. Kroll, M. R. Canagaratna, D. R. Worsnop, P.
676 K. Quinn, and T. S. Bates; 2011: Springtime Arctic haze contributions of submicron
677 organic particles from European and Asian combustion sources. *J. Geophys. Res.*, **116**,
678 doi: 10.1029/2010jd015178.

679 Fürst, J. J., H. Goelzer, and P. Huybrechts, 2015: Ice-dynamic projections of the Greenland ice
680 sheet in response to atmospheric and oceanic warming. *The Cryosphere*, **9**, 1039-1062,
681 doi:10.5194/tc-9-1039-2015.

682 Fürst, J. J., G. Durand, F. Gillet-Chaulet, L. Tavard, M. Rankl, M. Braun, and O. Gagliardini,
683 2016: The safety band of Antarctic ice shelves. *Nature Climate Change*, **6**, 479-482,
684 doi:10.1038/NCLIMATE2912.

685 Gorodetskaya, I. V., S. Kneifel, M. Maahn, K. Van Tricht, W. Theiry, J. H. Schween, A.
686 Mangold, S. Crewell, and N. P. M. Van Lipzig, 2015: Cloud and precipitation properties
687 from ground-based remote-sensing instruments in East Antarctica. *The Cryosphere*, **9**,
688 285-304, doi:10.5194/tc-9-285-2015.

689 Grazioli, J., J.-B. Madeleine, H. Gallée, R. M. Forbes, C. Genthon, G. Krinner, and A. Berne,
690 2017: Katabatic winds diminish precipitation contribution to the Antarctic ice mass
691 balance. *PNAS*, doi:10.1073/pnas.1707633114.

692 Hersbach, H., and D. Dee, 2016: ERA5 reanalysis is in production. *ECMWF Newsletter*, 147(7),
693 [https://www.ecmwf.int/sites/default/files/elibrary/2016/16299-newsletter-no147-spring-](https://www.ecmwf.int/sites/default/files/elibrary/2016/16299-newsletter-no147-spring-2016.pdf)
694 [2016.pdf](https://www.ecmwf.int/sites/default/files/elibrary/2016/16299-newsletter-no147-spring-2016.pdf).

695 Hines, K. M., and D. H. Bromwich, 2017: Simulation of late summer Arctic clouds during
696 ASCOS with Polar WRF. *Mon. Wea. Rev.*, **145**, 521-541, doi: 10.1175/MWR-D-16-
697 0079.1.

698 Hines, K. M., D. H. Bromwich, S.-H. Wang, I. Silber, J. Verlinde, and D. Lubin, 2019:
699 Microphysics of summer clouds in central West Antarctica simulated by Polar WRF and
700 AMPS. *Atmos. Chem. Phys.*, doi:10.5194/acp-2018-1251, accepted.

701 Hu, X., S. A. Sejas, M. Cai, Z. Li, and S. Yang, 2019: Atmospheric dynamics footprint on the
702 January 2016 ice sheet melting in West Antarctica. *Geophys. Res. Lett.*, **46**, 2829– 2835.
703 <https://doi.org/10.1029/2018GL081374>.

704 Hyder, P., and Coauthors, 2018: Critical Southern Ocean climate model biases traced to
705 atmospheric model cloud errors. *Nat. Commun.*, **9**, 3625, doi:10.1038/s41467-018-05634-
706 2.

707 Jenkins, A., D. Shoosmith, P. Dutrieux, S. Jacobs, T. W. Kim, S. H. Lee, H. K. Ha, and S.
708 Stammerjohn, 2018: West Antarctic Ice Sheet retreat in the Amundsen Sea driven by
709 decadal oceanic variability. *Nat. Geosci.*, **11**, 733-738, [https://doi.org/10.1038/s41561-](https://doi.org/10.1038/s41561-018-0207-4)
710 [018-0207-4](https://doi.org/10.1038/s41561-018-0207-4).

711 Jolly, B., P. Kuma, A. McDonald, A., and S. Parsons, 2018: An analysis of the cloud
712 environment over the Ross Sea and Ross Ice Shelf using CloudSat/CALIPSO satellite
713 observations: the importance of synoptic forcing. *Atmos. Chem. Phys.*, **18**(13), 9723–
714 9739. <https://doi.org/10.5194/acp-18-9723-2018>.

715 Joughin, I., B. E. Smith, and B. Medley, 2014: Marine ice sheet collapse potentially under way
716 for the Thwaites Glacier Basin, West Antarctica. *Science*, **344**, 735-738,
717 doi:10.1126/science.1249055.

718 Kingslake, J., J. C. Ely, I. Das, and R. E. Bell, 2017: Widespread movement of meltwater onto and
719 across Antarctic ice shelves. *Nature*, **544**, 349-352, doi:10.1038/nature22049.

720 Kneifel, S., M. S. Kulie, and R. Bennartz, 2011: A triple-frequency approach to retrieve
721 microphysical snowfall parameters. *J. Geophys. Res.*, **116** (D11203),
722 doi:10.1029/2010JD015430.

723 Kneifel, S., A. von Lerber, J. Tiira, D. Moisseev, P. Kollias, and J. Leinonen, 2015: Observed
724 relations between snowfall microphysics and triple-frequency radar measurements. *J.*
725 *Geophys. Res.*, **120**, 6034-6055, doi:10.1002/2015JD023156.

726 Kulie, M. S., M. J. Hiley, R. Bennartz, S. Kneifel, and S. Tanelli, 2014: Triple-frequency radar
727 reflectivity signatures of snow: Observations and comparisons with theoretical ice
728 particle scattering models. *J. Appl. Meteorol. Climatol.*, **53**, 1080–1098,
729 <http://dx.doi.org/10.1175/JAMC-D-13-066.1>.

730 Lachlan-Cope, T., C. Listowski, and S. O’Shea, 2016: The microphysics of clouds over the
731 Antarctic Peninsula – Part 1: Observations. *Atmos. Chem. Phys.*, **16**, 15605-15617,
732 doi:10.5194/acp-16-15605-2016.

733 Law, K. S., and A. Stohl, 2007: Arctic air pollution: Origins and impacts, *Science*, **315**(5818),
734 1537–1540, doi:10.1126/science.1137695.

735 Lawson, R. P., and A. Gettelman, 2014: Impact of Antarctic mixed-phase clouds on climate.
736 *PNAS*, **111**, 18156-18161, doi:10.1073/pnas.1418197111.

737 Lazzara, M. A., G. A. Weidner, L. M. Keller, J. E. Thom, and J. J. Cassano, 2012: Antarctic

738 automatic weather station program: 30 years of polar observations. *Bull. Amer. Meteorol.*
739 *Soc.*, **93**, 1519-1537, doi:10.1175/BAMS-D-11-00015.1.

740 Leaitch, W. R., and Coauthors, 2018: Organic functional groups in the submicron aerosol at 82.5
741 degrees N, 62.5 degrees W from 2012 to 2014. *Atmos. Chem. Phys.* **18**(5), 3269-3287.
742 doi:10.5194/acp-18-3269-2018.

743 Legrand, M., F. Ducroz, D. Wagenbach, R. Mulvaney, and J. Hall, 1998: Ammonium in coastal
744 Antarctic aerosol and snow: Role of polar ocean and penguin emissions, *J. Geophys.*
745 *Res.*, **103**, 11043–11056, <https://doi.org/10.1029/97jd01976>.

746 Legrand, M., V. Gros, S. Preunkert, R. Sarda-Esteve, A. M. Thierry, G. Pepy, and B. Jourdain,
747 2012: A reassessment of the budget of formic and acetic acids in the boundary layer at
748 Dumont d'Urville (coastal Antarctica): The role of penguin emissions on the budget of
749 several oxygenated volatile organic compounds, *J. Geophys. Res.*, **117**, D06308,
750 <https://doi.org/10.1029/2011jd017102>, 2012.

751 Leinonen, J. and D. Moisseev, 2015: What do triple-frequency radar signatures reveal about
752 aggregate snowflakes? *J. Geophys. Res.*, **120**, 229–239, doi:10.1002/2014JD022072.

753 Leinonen, J., and Coauthors, 2018: Retrieval of snowflake microphysical properties from multi-
754 frequency radar observations. *Atm. Meas. Tech.*, **11**, 5471-5488,
755 <https://doi.org/10.5194/amt-2018-73>.

756 Liu, J., and Coauthors, 2018: High summertime aerosol organic functional group concentrations
757 from marine and seabird sources at Ross Island, Antarctica, during AWARE. *Atmos.*
758 *Chem. Phys.*, **18**(12), 8571-8587, doi: 10.5194/acp-18-8571-2018.

759 Ma, H.-Y., and Coauthors, 2015: An improved hindcast approach for evaluation and diagnosis of
760 physical processes in global climate models, *J. Adv. Model. Earth Syst.*, **7**, 1810–1827,

761 doi:10.1002/2015MS000490.

762 Maahn, M., C. Burgard, S. Crewell, I. V. Gorodetskaya, S. Kneifel, S. Lhermite, K. Van Tricht,
763 and N. P. M. van Lipzig, 2014: How does the spaceborne radar blind zone affect derived
764 surface snowfall statistics in polar regions? *J. Geophys. Res.*, **119**, 13604-13620,
765 doi:10.1002/2014JD022079.

766 Mason, S. L., C. J. Chiu, R. J. Hogan, D. Moisseev, and S. Kneifel, 2018: Retrievals of riming
767 and snow density from vertically pointing Doppler radars. *J. Geophys. Res.*, **123**, 13,
768 807–13,834, doi:10.1029/2018JD028603.

769 Mather, J. H., and J. W. Voyles, 2013: The ARM Climate Research Facility: A review of
770 structure and capabilities. *Bull. Amer. Meteor. Soc.*, March 2013, 377-392,
771 doi:10.1175/BAMS-D-11-00218.1.

772 Matrosov, S. Y., 1998: A dual-wavelength radar method to measure snowfall rate. *J. Appl.*
773 *Meteorol.*, **37** (11), 1510–1521.

774 McFarquhar, G. M., and Coauthors, 2011: Indirect and Semi-Direct Aerosol Campaign: The
775 impact of Arctic aerosols on clouds. *Bull. Amer. Meteor. Soc.*, February 2011, 184-201,
776 doi:10.1175/2010BAMS2935.1.

777 Monaghan, A. J., D. H., Bromwich, J. G. Powers, and K. W. Manning, 2005: The Climate of the
778 McMurdo, Antarctica, Region as Represented by One Year of Forecasts from the
779 Antarctic Mesoscale Prediction System. *J. Clim.*, **18**(8), 1174–1189.,
780 <https://doi.org/10.1175/JCLI3336.1>.

781 Morrison, H., J. A. Curry, and V. I. Khvorostyanov, 2005: A new double-moment microphysics
782 scheme for application in cloud and climate models. Part I: Description. *J. Atmos. Sci.*,
783 **62**, 1665–1677, doi:10.1175/JAS3446.1.

784 Morrison, H., G. de Boer, G. Feingold, J. Harrington, M. D. Shupe, and K. Sulia, 2011:
785 Resilience of persistent Arctic mixed-phase clouds. *Nat. Geosci.*, **5**,
786 doi:10.1038/NGEO1332

787 Nicolas, J. P., and D. H. Bromwich, 2011: Climate of West Antarctica and influence of marine air
788 intrusions. *J. Climate*, **24**, 49-67, doi: 10.1175/2010JCLI3522.1.

789 Nicolas, J. P., and D. H. Bromwich, 2014: New reconstruction of Antarctic near-surface
790 temperatures: Multidecadal trends and reliability of global reanalyses. *J. Clim.*, **27**, 8070-
791 8093, doi:10.1175/JCLI-D-13/00733.1.

792 Nicolas, J. P., and Coauthors, 2017: January 2016 extensive summer melt in West Antarctica
793 favored by strong El Niño, *Nature Commun.*, **8**:15799, doi: 10.1038/ncomms15799.

794 Nigro, M. A., and J. J. Cassano, 2014: Analysis of the Ross Ice Shelf airstream forcing
795 mechanisms using self-organizing maps. *Mon. Weather Rev.*, **142**, 4719-4734,
796 doi:10.1175/MWR-D-14-00077.1.

797 Oppenheimer, M., 1998: Global warming and the stability of the West Antarctic Ice Sheet.
798 *Nature*, **393**, 325-332, <http://dx.doi.org/10.1038/30661>.

799 Paolo, F. S., H. A. Fricker, and L. Padman, 2015: Volume loss from Antarctic ice shelves is
800 accelerating. *Science*, **348**, 327-330, doi:10.1126/science.aaa0940.

801 Peppler, R. A., and Coauthors, 2008: An overview of ARM Program Climate Research Facility
802 data quality assurance. *The Open Atmospheric Science Journal*, **2**, 192-216,
803 <https://benthamopen.com/contents/pdf/TOASCJ-2-192.pdf>

804 Petäjä, T., and Coauthors, 2016: BA ECC: A Field Campaign to Elucidate the Impact of Biogenic
805 Aerosols on Clouds and Climate, *Bull. Amer. Meteor. Soc.*, **97**, 1909–1928,
806 doi:10.1175/BAMS-D-14-00199.1.

807 Pollard, D., R. M. DeConto, and R. B. Alley, 2015: Potential Antarctic ice sheet retreat driven by
808 hydrofracturing and ice cliff failure. *Earth and Planetary Science Letters*, **412**, 112-121,
809 <http://dx.doi.org/10.1016/j.epsl.2014.12.035>.

810 Pritchard, H. D., S. R. M. Ligtenberg, H. A. Fricker, D. G. Vaughan, M. R. van den Broeke, and
811 L. Padman, 2012: Antarctic ice-sheet loss driven by basal melting of ice shelves. *Nature*,
812 **484**, 502-505, doi:10.1038/nature10968.

813 Quinn, P. K., T. L. Miller, T. S. Bates, J. A. Ogren, E. Andrews, and G. E. Shaw, 2002: A 3-year
814 record of simultaneously measured aerosol chemical and optical properties at Barrow,
815 Alaska. *J. Geophys. Res.*, **107**(D11), doi:10.1029/2001JD001248.

816 Quinn, P. K., G. E. Shaw, E. Andrews, E. G. Dutton, T. Ruoho - Airola, and S. L. Gong, 2007:
817 Arctic haze: Current trends and knowledge gaps, *Tellus, Ser. B*, **59**(1), 99–114,
818 doi:10.1111/j.1600-0889.2006.00238.x.

819 Rasch, P. J., S. Xie, P.-L. Ma, W. Lin, H. Wang, Q. Tang, and Coauthors, 2019: An overview of
820 the atmospheric component of the Energy Exascale Earth System Model. *J. Adv. Mod.*
821 *Earth Sys.*, **11**, <https://doi.org/10.1029/2019MS001629>.

822 Ricaud, P., E. Bazile, M. del Guasta, C. Lanconelli, P. Grignioni, and A. Mahjoub, 2017:
823 Genesis of diamond dust, ice fog and thick cloud episodes observed and modeled above
824 Dome C, Antarctica. *Atmos. Chem. Phys.*, **17**, 5221-5237, doi:10.5194/acp-17-5221-
825 2017.

826 Rignot, E., J. Mouginot, M. Morlighem, H. Seroussi, and B. Scheuchl, 2014: Widespread, rapid
827 grounding line retreat of Pine Island, Thwaites, Smith, and Kohler glaciers, West
828 Antarctica, from 1992-2011. *Geophys. Res. Lett.*, **41**, 3502-3509,
829 doi:10.1002/2014GL060140.

830 Rowe, P. M., C. J. Cox, S. Neshyba, and V. P. Walden, 2019: Toward autonomous surface-based
831 infrared remote sensing of polar clouds: Retrievals of cloud microphysical properties,
832 *Atmos. Meas. Tech.*, **12**, 5071-5086, <https://doi.org/10.5195.amt-12-5071-2019>.

833 Scambos, T. A., C. Hulbe, M. Fahnestock, and J. Bohlander, 2000: The link between climate
834 warming and break-up of ice shelves in the Antarctic Peninsula. *J. Glaciol.*, **46**, 516-530,
835 <https://doi.org/10.3189/172756500781833043>.

836 Schmale, J., and Coauthors, 2013: Sub-Antarctic marine aerosol: dominant contributions from
837 biogenic sources, *Atmos. Chem. Phys.*, **13**, 8669–8694, [https://doi.org/10.5194/acp-13-](https://doi.org/10.5194/acp-13-8669-2013)
838 8669-2013.

839 Schmidt, G. A., and Coauthors, 2014: Configuration and assessment of the GISS ModelE2
840 contributions to the CMIP5 archive. *J. Adv. Model. Earth Syst.*, **6**, no. 1, 141-184,
841 [doi:10.1002/2013MS000265](https://doi.org/10.1002/2013MS000265).

842 Schneider, D. P., C. Deser, and Y Okumura, 2012: An assessment and interpretation of the
843 observed warming of West Antarctica in the austral spring. *Clim. Dyn.*, **38**, 323-347,
844 [doi:10.1007/s00382-0101-0985-x](https://doi.org/10.1007/s00382-0101-0985-x).

845 Scott, R. C., and D. Lubin, 2014: Mixed-phase cloud radiative properties over Ross Island: The
846 influence of various synoptic-scale atmospheric circulation regimes, *J. Geophys. Res.*,
847 **119**, [doi:10.1002/2013JD021132](https://doi.org/10.1002/2013JD021132).

848 Scott, R. C., and D. Lubin, 2016: Unique manifestations of mixed-phase cloud properties over
849 Ross Island and the Ross Ice Shelf, Antarctica. *Geophys. Res. Lett.*, **43**, 2936-2945,
850 [doi:10.1002/2015GL067246](https://doi.org/10.1002/2015GL067246).

851 Scott, R. C., J. P. Nicolas, D. H. Bromwich, J. R. Norris, and D. Lubin, 2019: Meteorological
852 drivers and large-scale climate forcing of West Antarctic surface melt. *J. Clim.*, **32**, 665-
853 683, doi:10.1175/JCLI-D-18-023.1.

854 Shaw, P. M., L. M. Russell, A. Jefferson, and P. K. Quinn, 2010: Arctic organic aerosol
855 measurements show particles from mixed combustion in spring haze and from frost
856 flowers in winter. *Geophys. Res. Lett.* **37**, doi: 10.1029/2010gl042831.

857 Shaw, G. E., 1982: Evidence for a central Eurasian source area of Arctic haze in Alaska, *Nature*,
858 **299**(5886), 815–818, doi:10.1038/299815a0.

859 Shupe, M. D. (2011). Clouds at Arctic Atmospheric Observatories. Part II: Thermodynamic
860 Phase Characteristics. *J. Appl. Meteor. Clim.*, *50*(3), 645–661.
861 <https://doi.org/10.1175/2010JAMC2468.1>

862 Silber, I., J. Verlinde, E. W. Eloranta, and M. Cadetdu, 2018a: Antarctic cloud macrophysical,
863 thermodynamic phase, and atmospheric inversion coupling properties at McMurdo
864 Station: 1. Principal data processing and climatology. *J. Geophys. Res.*, *123*, 6099-6121,
865 <https://doi.org/10.1029/2018JD028279>.

866 Silber, I., J. Verlinde, E. W. Eloranta, C. J. Flynn, & D. M. Flynn, 2018b: Polar liquid cloud base
867 detection algorithms for high spectral resolution or micropulse lidar data. *J. Geophys.*
868 *Res.* <https://doi.org/10.1029/2017JD027840>.

869 Silber, I., Verlinde, J., Cadetdu, M., Flynn, C. J., Vogelmann, A. M., & Eloranta, E. W., 2019a:
870 Antarctic cloud macrophysical, thermodynamic phase, and atmospheric inversion
871 coupling properties at McMurdo Station. Part II: Radiative impact during different
872 synoptic regimes. *J. Geophys. Res.* <https://doi.org/10.1029/2018JD029471>.

873 Silber, I., A. M. Fridlind, J. Verlinde, A. S. Ackerman, Y.-S. Chen, D. H. Bromwich, S.-H.

874 Wang, M. Cadetdu, and E. W. Eloranta, 2019b: Persistent supercooled drizzle at
875 temperatures below -25°C observed at McMurdo Station, Antarctica, *J. Geophys. Res.*,
876 doi:10.1029/2019JD030882, in press.

877 Silber, I., J. Verlinde, S.-H. Wang, D. H. Bromwich, A. M. Fridlind, M. Cadetdu, and E. W.
878 Eloranta, 2019c: Cloud influence on ERA5 and AMPS surface downwelling longwave
879 radiation biases in West Antarctica. *J. Climate*, <https://doi.org/10.1175/JCLI-D-19->
880 0149.1.

881 Skamarock, W. C., and Coauthors, 2008: *A description of the Advanced Research WRF version*
882 3. NCAR Tech. Note NCAR/TN-475+STR, 113 pp.,
883 <https://doi.org/10.5065/D68S4MVH>.

884 Snider, J. R., D. Leon, and Z. Wang, 2017: Droplet concentration and spectral broadening in
885 Southeast Pacific stratocumulus clouds. *J. Atmos. Sci.*, **74**, 719-749,
886 <https://doi.org/10.1175/JAS-D-16-0043.1>.

887 Stein, T. H. M., C. D. Westbrook, and J. C. Nicol, 2015: Fractal geometry of aggregate
888 snowflakes revealed by triple-wavelength radar measurements. *Geophys. Res. Lett.*, **42**,
889 176–183, doi:10.1002/2014GL062170.

890 Town, M. S., V. P. Walden, and S. G. Warren, 2007: Cloud cover over the South Pole from
891 visual observations, satellite retrievals, and surface-based infrared radiation
892 measurements. *J. Climate*, **20**, 544-559.

893 Trenberth, K. E., and J. T. Fasullo, 2010: Simulation of present day and twenty first century
894 energy budgets of the Southern Oceans. *J. Climate*, **23**, 440-454,
895 doi:10.1175/2009JCLI3152.1

896 Tridon, F., et al., 2019: The microphysics of stratiform precipitation during OLYMPEX:
897 compatibility between 3-frequency radar and airborne in situ observations. *J. Geophys.*
898 *Res.*, in review.

899 Turner, D. D., 2005: Arctic mixed-phase cloud properties from AERI-lidar observations:
900 Algorithm and results from SHEBA. *J. Appl. Meteorol.*, **44**, 427-444,
901 doi:10.1175/JAM2208.1.

902 Verlinde, J., and Coauthors, 2007: The Mixed-Phase Arctic Cloud Experiment, *Bull. Amer.*
903 *Meteor. Soc.*, **88**, 205-221, doi:10.1175/BAMS-88-2-205.

904 Walden, V. P., W. L. Roth, R. S. Stone, and B. Halter, 2006: Radiometric validation of the
905 Atmospheric Infrared Sounder over the Antarctic Plateau. *J. Geophys. Res.*, **111**,
906 D09S03, doi:10.1029/2005JD006357.

907 Weertman, J., 1974: Stability of the junction of an ice sheet and an ice shelf. *J. Glaciol.*, **13**, 3-
908 11, <https://doi.org/10.3189/S0022143000023327>.

909 Wilson, A., R. C. Scott, M. P. Cadeddu, V. Ghate, and D. Lubin, 2018: Cloud optical properties
910 over West Antarctica from shortwave spectroradiometer measurements during AWARE.
911 *J. Geophys. Res.*, **123**, doi:10.1029/2018JD028347.

912 Xu, L., L. M. Russell, R. C. J. Somerville, and P. K. Quinn, 2013: Frost flower aerosol effects on
913 Arctic wintertime longwave cloud radiative forcing. *J. Geophys. Res.*, **118**, 13282-13291,
914 doi: 10.1002/2013jd020554.

915 Xu, L., L. M. Russell, and S. M. Burrows, 2016: Potential sea salt aerosol sources from frost
916 flowers in the pan-Arctic region. *J. Geophys. Res.*, **121**(18), 10840-10856, doi:
917 10.1002/2015jd024713.

918 Xu, J.-X, and Coauthors: 2017: Source attribution of Arctic black carbon constrained by aircraft
919 and surface measurements. *Atm. Chem. Phys.*, **17**, 11971-11989, doi:10.5194/acp-17-
920 11971-2017.

921 Zhang, D., A. M. Vogelmann, P. Kollias, E. P. Luke, F. Yang, D. Lubin, and Z. Wang, 2019:
922 Comparison of Antarctic and Arctic Stratiform Mixed-phase Cloud Properties Using
923 Ground-based Remote Sensing Measurements, *J. Geophys. Res.*, *124*,
924 <https://doi.org/10.1029/2019JD030673>.

925 Zou, X., D. H. Bromwich, J. P. Nicolas, A. Montenegro, and S.-H. Wang, 2019: West Antarctic
926 surface melt event of January 2016 facilitated by foehn warming. *Q. J. R. Meteorol. Soc.*,
927 **145**, 687-704, doi: 10.1002/qj.3460.

928 Zwally, H. J., M. B. Giovinetto, J. Li, H. G. Cornejo, M. A. Beckley, A. Brenner, J. L. Saba, and
929 D. Yi, 2005: Mass changes of the Greenland and Antarctic ice sheets and shelves and
930 contributions to sea-level rise: 1992-2002. *J. Glaciol.*, **51**, 509-527,
931 <https://doi.org/10.3189/172756505781829007>.

Table 1. Instruments Deployed to Ross Island (McMurdo Station CosRay Site). Instruments marked with an asterisk are deployed first at WAIS Divide December 2015-January 2016 then redeployed to CosRay for the remainder of the field program.

Instrument Name	Instrument Acronym	Quantities Measured
X-band and Ka-band scanning ARM cloud radar	X/KA-SACR	Co- and cross-polar radar Doppler spectrum and moments (reflectivity, Doppler velocity, spectrum width, linear depolarization ratio, differential reflectivity)
Scanning W-band ARM cloud radar	SWACR	Radar Doppler spectrum and moments
Ka-band ARM zenith radar	KAZR	Radar Doppler spectrum and moments at high (30 m) range resolution
Atmospheric Emitted Radiance Interferometer	AERI	Absolute thermal infrared spectral radiance emitted by the atmosphere down to the instrument
High spectral resolution lidar	HSRL	Aerosol optical depth, volume backscatter, cross section, cloud and aerosol depolarization
Micropulse lidar	MPL	Altitude of cloud layers
Vaisala ceilometer	VCEIL	Cloud base height
Beam-steerable radar wind profiler	RWP	Wind and virtual temperature profiles
Parsivel optical disdrometer	PARSIVEL	Precipitation particle size distribution and fall speed
Cloud condensation nuclei counter	CCN	Cloud condensation nuclei as function of supersaturation
Condensation particle counter	CPC	Total aerosol particle concentration down to diameter 10 nm
Hygroscopic tandem differential mobility analyzer	HTDMA	Aerosol size, mass, or number distribution as function of RH
Ambient nephelometer	NEPH AMB	Aerosol light scattering coefficient at ambient RH
Dry nephelometer	NEPH DRY	Dry aerosol light scattering coefficient
Ozone	O3	Ozone concentration
Particle soot absorption photometer	PSAP	Optical transmittance of aerosol particles
Aerosol filter sampling (SIO)	AER FLTR	Aerosol chemical composition by FTIR and XRF

Upward-looking precision spectral pyranometer	SKYRAD PSP	Downwelling total shortwave irradiance
Upward-looking Eppley model 8-48 diffuse pyranometer	SKYRAD 8-48	Downwelling diffuse shortwave irradiance
Upward-looking precision infrared radiometer	SKYRAD PIR	Downwelling longwave irradiance
Upward-looking Infrared thermometer	SKYRAD IRT	Sky equivalent blackbody temperature
Downward-looking precision spectral pyranometer	GRNDRAD PSP	Upwelling shortwave radiation reflected by surface
Downward-looking precision infrared radiometer	GRNDRAD PIR	Upwelling longwave radiation emitted by surface
Downward-looking Infrared thermometer	GRNDRAD IRT	Surface equivalent blackbody temperature
Cimel sunphotometer	CSPHOT	Multispectral direct solar irradiances
Multifilter rotating shadowband radiometer	MFRSR	Direct normal, diffuse horizontal, and total horizontal irradiances at six standard wavelengths
(*) Analytical Spectral Devices FieldSpec Pro shortwave spectroradiometer (SIO)	(*) ASD	Downwelling spectral shortwave irradiance 350-2200 nm
Eddy correlation flux measurement system	ECOR	Surface turbulent fluxes of momentum, sensible heat, latent heat, and carbon dioxide
Total sky imager	TSI	Cloud fraction
Vaisala present weather detector	PWD	Visibility, precipitation detection
(*) G-band vapor radiometer	(*) GVRP	High-time-resolution water vapor and temperature profiling, and column-integrated liquid water and water vapor
Microwave radiometer, two channel	MWR, 2C	Column-integrated liquid water and water vapor
Balloon-borne sounding system	SONDE	Vertical profiles of T, P, RH, wind speed and direction
Meteorological instrumentation at AMF	MET	Near-surface (2 m) T, P, RH, wind speed and direction
Local meteorology at top of AOS stack	AOS MET	Wind speed, direction, T, RH, P

Table 2. Instruments Deployed to the WAIS Divide Ice Camp.

Instrument Name	Instrument Acronym	Quantities Measured
-----------------	--------------------	---------------------

Upward-looking precision spectral pyranometer	SKYRAD PSP	Downwelling total shortwave irradiance
Upward-looking Eppley model 8-48 diffuse pyranometer	SKYRAD 8-48	Downwelling diffuse shortwave irradiance
Upward-looking precision infrared radiometer	SKYRAD PIR	Downwelling longwave irradiance
Upward-looking Infrared thermometer	SKYRAD IRT	Sky equivalent blackbody temperature
Downward-looking precision spectral pyranometer	GRNDRAD PSP	Upwelling shortwave radiation reflected by surface
Downward-looking precision infrared radiometer	GRNDRAD PIR	Upwelling longwave radiation emitted by surface
Downward-looking Infrared thermometer	GRNDRAD IRT	Surface equivalent blackbody temperature
Cimel sunphotometer	CSPHOT	Multispectral direct solar irradiances
Multifilter rotating shadowband radiometer	MFRSR	Direct normal, diffuse horizontal, and total horizontal irradiances at six standard wavelengths
Analytical Spectral Devices FieldSpec Pro shortwave spectroradiometer (SIO)	ASD	Downwelling spectral shortwave irradiance 350-2200 nm (Lubin)
Eddy correlation flux measurement system	ECOR	Surface turbulent fluxes of momentum, sensible heat, latent heat, and carbon dioxide
Total sky imager	TSI	Cloud fraction
Vaisala ceilometer	VCEIL	Cloud base height
Parsivel optical disdrometer	PARSIVEL	Precipitation particle size distribution and fall speed
Vaisala present weather detector	PWD	Visibility, precipitation detection
G-band vapor radiometer	GVRP	High-time-resolution water vapor and temperature profiling, and column-integrated liquid water and water vapor
Microwave radiometer, two channel	MWR, 2C	Column-integrated liquid water and water vapor
Balloon-borne sounding system	SONDE	Vertical profiles of T, P, RH, wind speed and direction
Meteorological instrumentation at AMF	MET	Near-surface (2 m) T, P, RH, wind speed and direction

Figure Captions

Figure 1. Map of West Antarctica, the Transantarctic Mountains, and the Ross Ice Shelf, showing the AWARE measurement locations at McMurdo Station and the WAIS Divide Ice Camp. The insert at the upper right indicates maritime regions Ross Sea (RS) and Bellingshausen Sea (BS) that influence moisture advection/cloud and clear skies over West Antarctica, respectively. Adapted from Nicolas and Bromwich (2011).

Figure 2. The AMF2 installation at the McMurdo Station CosRay site. Top: view of the entire site showing locations of adjacent meteorological and radar calibration target towers, and the southerly view of the scanning radars. Bottom: detail of instrument installation within the AMF2.

Figure 3. The AWARE surface energy budget equipment at WAIS Divide. Top: view of the sea container housing most of the instruments, with the SKYRAD installation at the far right and Total Sky Imager, ceilometer and surface turbulent flux instruments at the far left. Bottom: detail of the instrument installation on the roof of the sea container.

Figure 4. Thirty-day (+1-hour) running-mean total hydrometeor and liquid-cloud occurrence fractions at McMurdo (solid) and Utqiagvik (dashed). The monthly-mean values are given by the filled markers. The months represented in each season here for McMurdo (Utqiagvik) are DJF (JJA) for summer, MAM (SON) for autumn, JJA (DJF) for winter, and SON (MAM) for spring. The temperature curve (based on sounding profiles) represents the average temperature between the surface and 4 km altitude. The x-axis ticks mark the 16th of each month at 00:00 UTC. The annual hydrometeor (liquid) occurrence fraction is higher by ~20% (~31%) at Utqiagvik relative to McMurdo.

Figure 5. Box and whisker diagrams of cloud (hydrometeor) thickness (top) and highest cloud top height (middle), and highest cloud top temperature (bottom), designating the median (thick dotted line), 1st and 3rd quartiles (box edges), 5th and 95th percentiles (whiskers), and mean (asterisk; values are provided in the parentheses).

Figure 6. Box and whisker diagram of cloud (top) and liquid-bearing (bottom) layer persistence. The total number of cloud (liquid) samples in each month are shown by the triangle markers. The bars represent the longest-lived liquid-bearing cloud layers observed in each season (values are provided in the parentheses; dashed red line denotes 24 h).

Figure 7. Lowest (per profile) liquid-bearing cloud layer base height box and whiskers diagram (top) and annual cumulative distribution function (bottom).

Figure 8. CCN and submicron aerosol particle mass concentrations during annual cycles measured at McMurdo Station, Antarctic: (A) CCN at 0.1% and 1% supersaturation and (B) organic, non-sea-salt sulfate (SO₄), sea salt, and non-sea-salt dust mass concentration (from Liu et al. 2018). Sea salt particle mass concentration was estimated as the sum of measured Na*1.47 and Cl based on Bates et al. 2012, and non-sea-salt sulfate (SO₄²⁻) mass concentration was scaled from XRF S after removing for sea-salt associated S (Liu et al. 2018). Non-sea-salt dust mass concentration was calculated from XRF metal concentrations, assuming dust consists of MgCO₃, Al₂O₃, SiO₂, K₂O, CaCO₃, TiO₂, Fe₂O₃, MnO, and BaO after removing sea-salt associated metal amounts (Liu et al. 2018). Lines show 5-parameter polynomial fits to 2016 measurements.

Figure 9. Submicron aerosol particle mass concentrations during annual cycles for the Arctic: (A) Organic, non-sea-salt sulfate (SO₄), and sea salt mass concentration measured at Utqiagvik, Alaska, by FTIR and IC (Shaw et al. 2010; Frossard et al. 2011; Quinn et al. 2002); (B) Organic, non-sea-salt sulfate (SO₄), and sea salt mass concentration measured at Alert,

Nunavut, by FTIR and IC (Leitch et al. 2018). Sea salt particle mass concentration was estimated as the sum of measured Na^+ and Cl^- based on Bates et al. 2012, and non-sea-salt sulfate (SO_4^{2-}) mass concentration was calculated from IC sulfate after removing for sea-salt associated SO_4 . Lines show 5-parameter polynomial fits to 2009 (Utqiagvik) and 2013 (Alert) measurements.

Figure 10. Box and whisker diagrams of submicron mass concentrations for (a) organic, (b) sea salt, and (c) non-sea salt sulfate, (d) CCN concentrations at 0.1% and 1%; designating the median (thick dotted line), 1st and 3rd quartiles (box edges), 5th and 95th percentiles (whiskers), and mean (asterisks). The McMurdo measurements are for 2016. The Utqiagvik mass and CCN concentrations are for 2009. The Utqiagvik CCN concentrations for 2009 were missing some supporting CN measurements so quality control was limited.

Figure 11. Two-dimensional histogram of DWR Ka-W versus DWR X-Ka measurements collected by the X-Ka and W-band ARM radars during 10 January 2016 at McMurdo Station. Negative DWRs are unexpected and might be caused by imperfect radar volume matching and measurement noise. Away from the Rayleigh region (black square) different growth regimes can be identified (continuous, dotted and dashed lines). The red arrow points towards ice particles characterized by higher densities and larger sedimentation velocities.

Figure 12. Multispectral characterization of mixed-phase clouds at McMurdo during AWARE (February 8, 2016) and at Utqiagvik, Alaska (December 28, 2015). Shown are time-height cross sections from zenith-pointing instruments: a,b) HSRL backscatter cross section (β), c,d) HSRL linear depolarization ratio, and e,f) Ka-band radar reflectivity (Z_e). Values for a-f are given by the color bars to the right of the panels. Panels g-m are retrievals of: g,h) optical depth (separately for ice and liquid phase), i,j) liquid water effective radius, k,l) ice particle effective

radius, and m,n) liquid water path (*LWP*). The retrievals use downwelling infrared spectral radiances measured by the AERI via the method of Rowe et al. (2019, submitted, and references within). Retrieval uncertainty is indicated by the vertical extent of the symbols, obtained from the square root of the diagonal of the error covariance matrix for the state variable plotted.

Figure 13. Simulation of the WAIS Divide melt event using Polar WRF (PWRF), using input from ERA-Interim (PWRF-EI) and GFS (PWRF-FNL), compared against AWARE observations from radiosondes and microwave radiometer measurements: (top) near surface (2-m) air temperature, (middle) cloud *LWP*, (bottom) vertically integrated PWV.

Figure 14. GCM evaluations at the WAIS Divide during the 2016 West Antarctic melt event for the DOE EAMv1 and GISS ModelE. EAMv1 simulations are run in hindcast mode (Ma et al. 2015) initialized using ERA5 (Hersbach and Dee 2016) with the 12-36 h hindcast period shown here. The GISS ModelE simulation is nudged to ERA5. The EAMv1 (red) and ModelE (blue) simulations are compared with observations (black) of (a) PWV, and (b) cloud *LWP*, both retrieved from surface microwave radiometer data. The primary warming period is indicated by gray shading. Model-observation differences for net surface fluxes are shown for (c) total net radiation (longwave plus shortwave), (d) total turbulence (sensible and latent heat, with the sign being positive towards the atmosphere), and (e) total energy into the snowpack. (f) Shows a scatter plot of the model-observation differences in net longwave flux at the surface (LW) versus differences in *LWP*. The observational data in (a)-(f) are described in Nicholas et al. (2017).

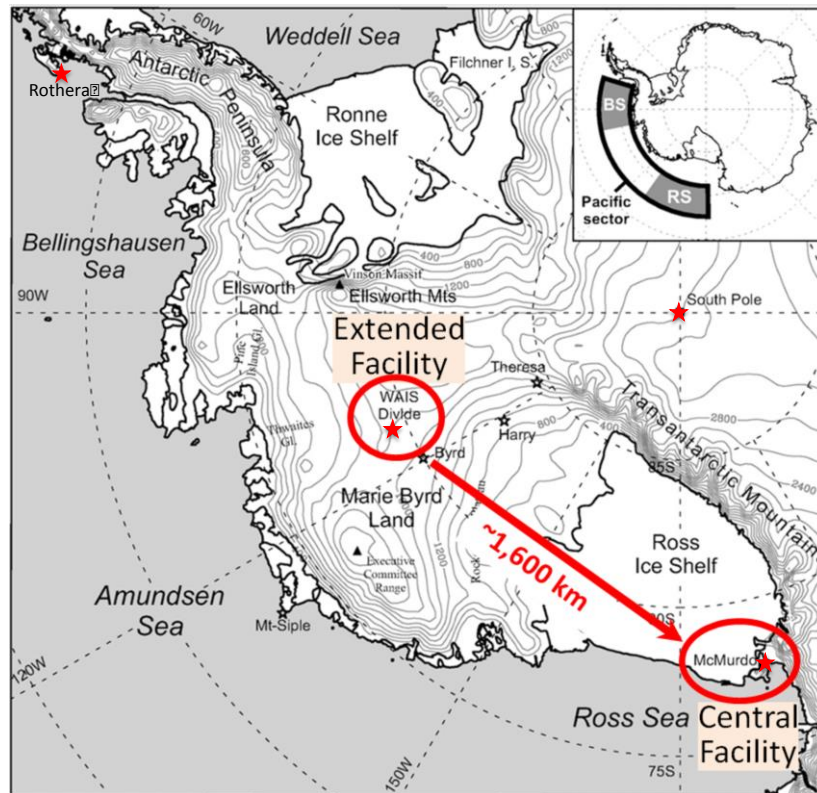


Figure 1. Map of West Antarctica, the Transantarctic Mountains, and the Ross Ice Shelf, showing the AWARE measurement locations at McMurdo Station and the WAIS Divide Ice Camp. The insert at the upper right indicates maritime regions Ross Sea (RS) and Bellingshausen Sea (BS) that influence moisture advection/cloud and clear skies over West Antarctica, respectively. Adapted from Nicolas and Bromwich (2011).



Figure 2. The AMF2 installation at the McMurdo Station CosRay site. Top: view of the entire site showing locations of adjacent meteorological and radar calibration target towers, and the southerly view of the scanning radars. Bottom: detail of instrument installation within the AMF2.

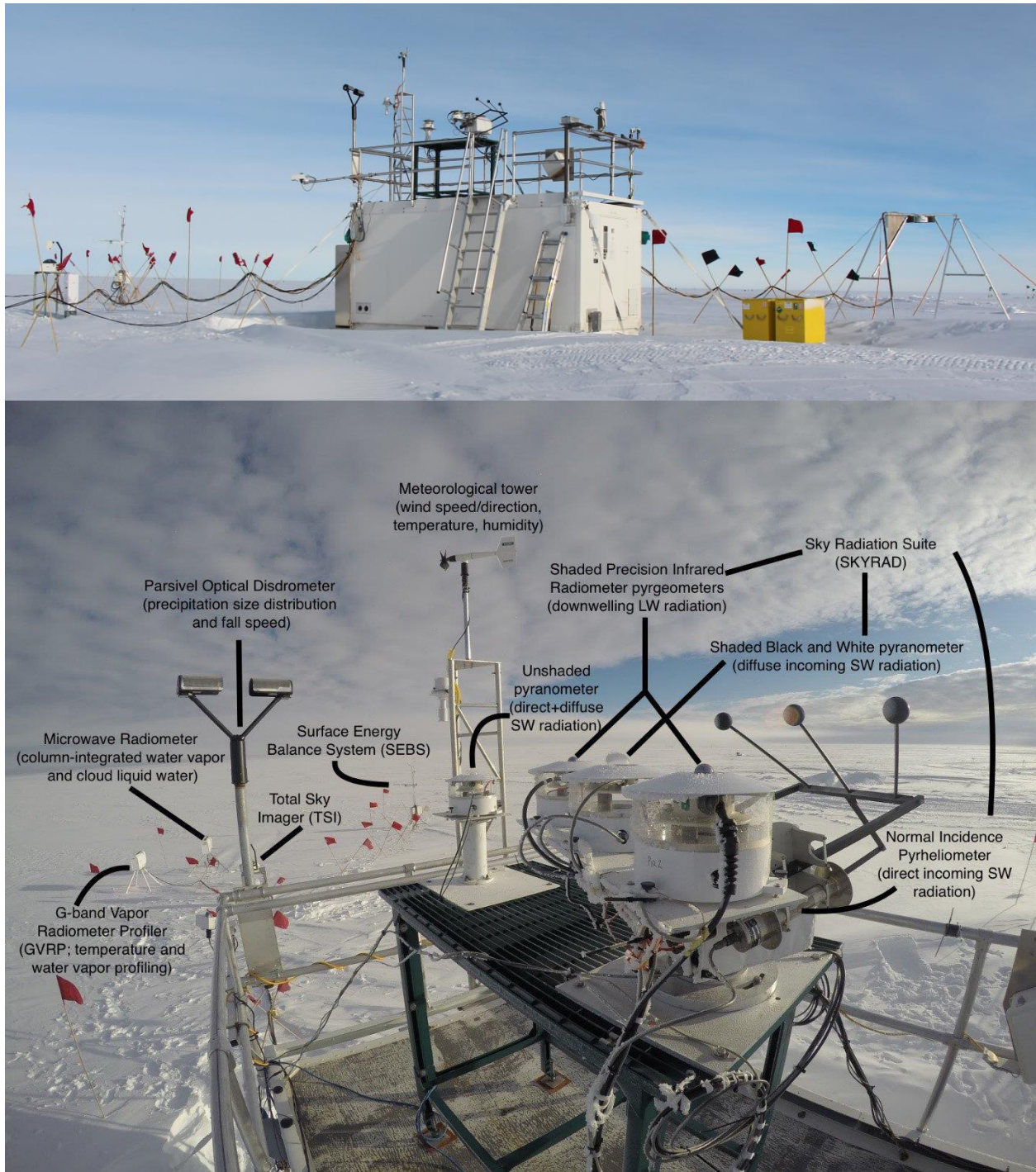


Figure 3. The AWARE surface energy budget equipment at WAIS Divide. Top: view of the sea container housing most of the instruments, with the SKYRAD installation at the far right and Total Sky Imager, ceilometer and surface turbulent flux instruments at the far left. Bottom: detail of the instrument installation on the roof of the sea container.

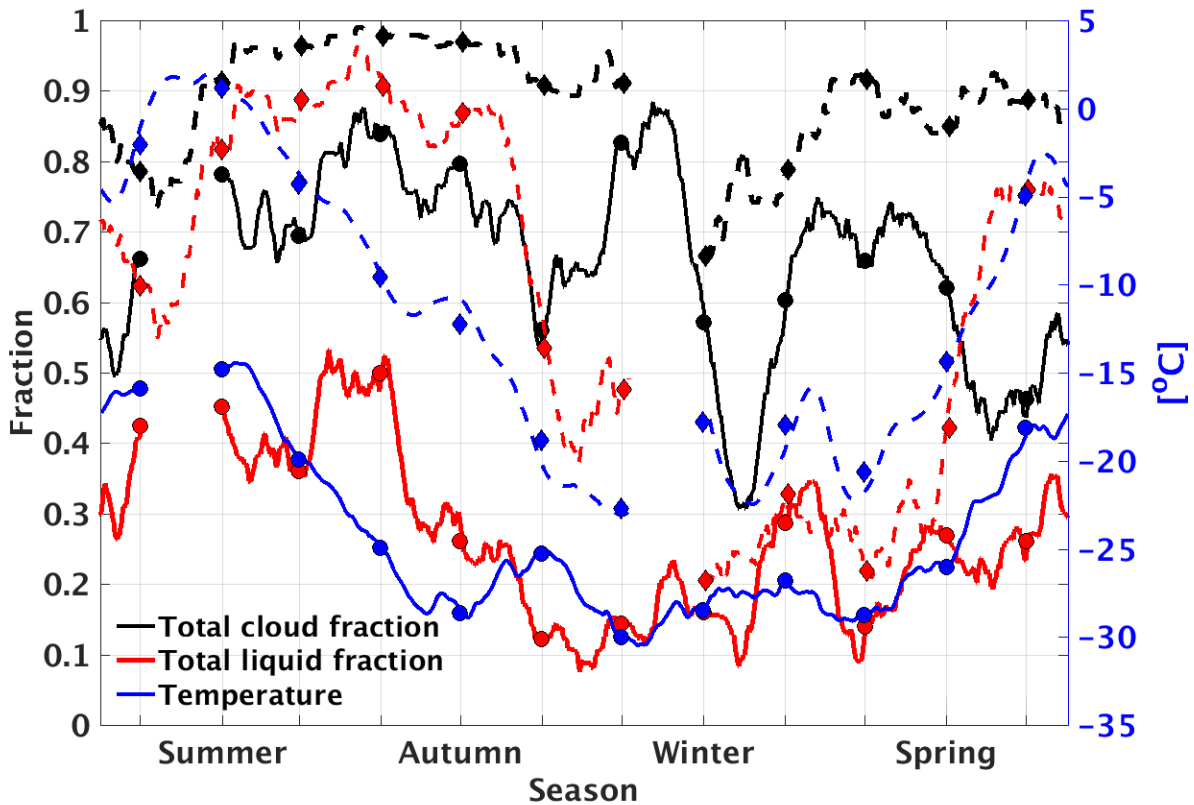


Figure 4. Thirty-day (+1-hour) running-mean total hydrometeor and liquid-cloud occurrence fractions at McMurdo (solid) and Utqiagvik (dashed). The monthly-mean values are given by the filled markers. The months represented in each season here for McMurdo (Utqiagvik) are DJF (JJA) for summer, MAM (SON) for autumn, JJA (DJF) for winter, and SON (MAM) for spring. The temperature curve (based on sounding profiles) represents the average temperature between the surface and 4 km altitude. The x-axis ticks mark the 16th of each month at 00:00 UTC. The annual hydrometeor (liquid) occurrence fraction is higher by ~20% (~31%) at Utqiagvik relative to McMurdo.

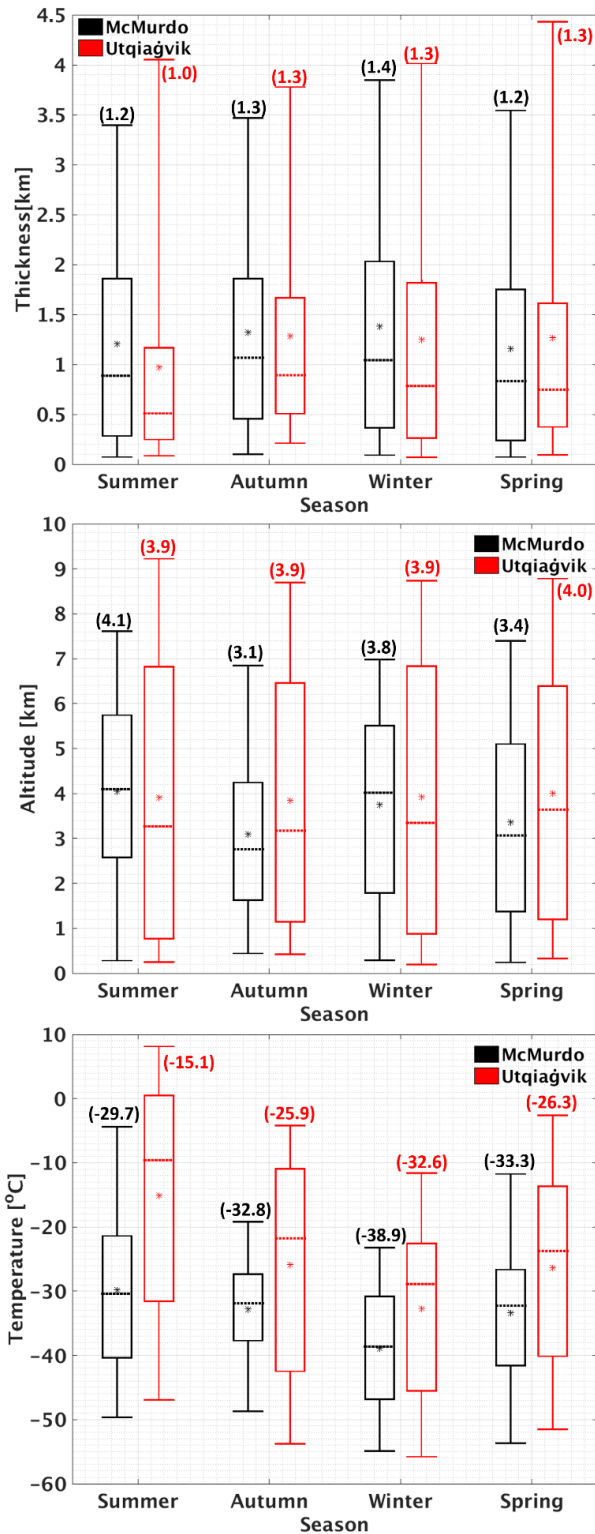


Figure 5. Box and whisker diagrams of cloud (hydrometeor) thickness (top) and highest cloud top height (middle), and highest cloud top temperature (bottom), designating the median (thick dotted line), 1st and 3rd quartiles (box edges), 5th and 95th percentiles (whiskers), and mean (asterisk; values are provided in the parentheses).

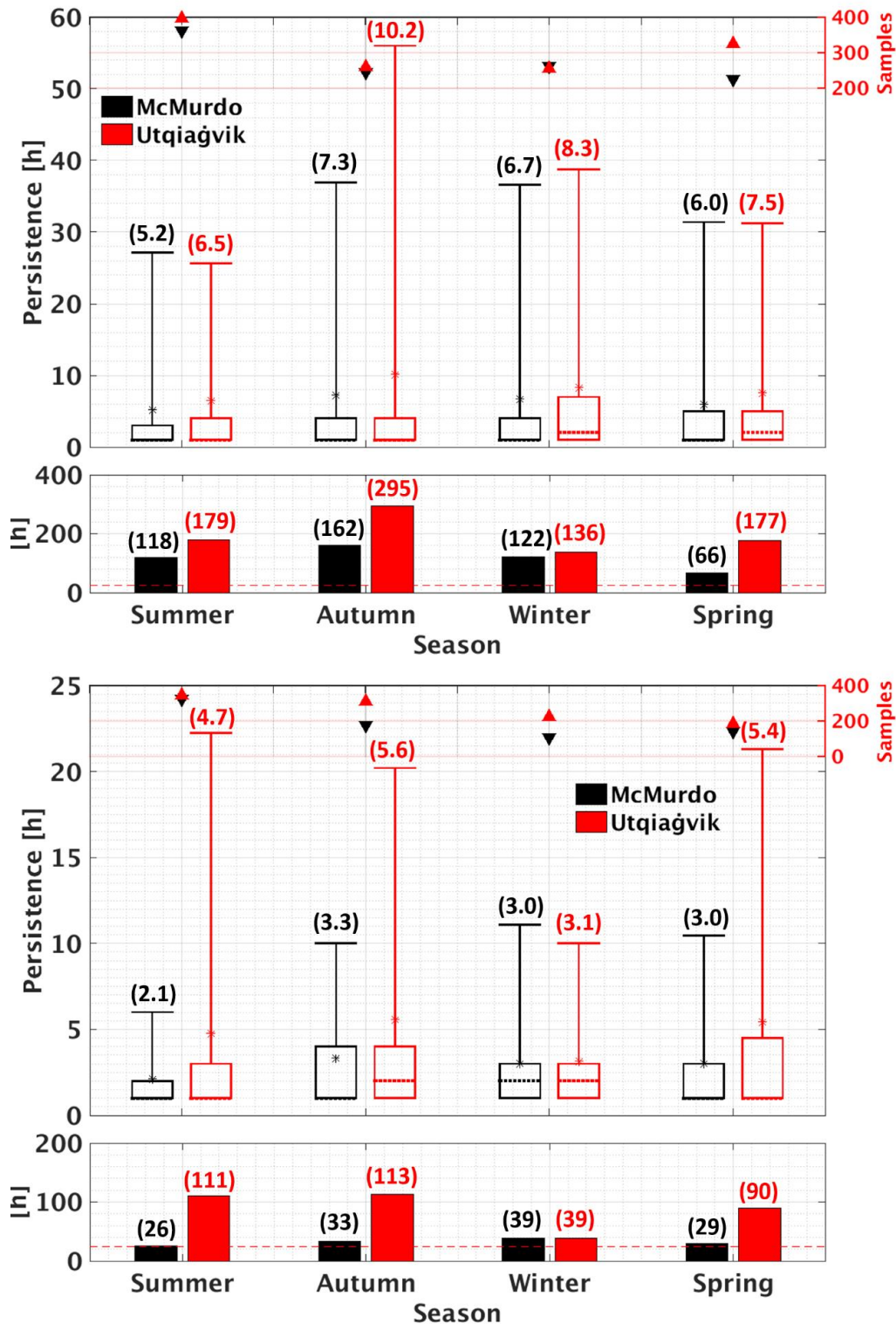


Figure 6. Box and whisker diagram of cloud (top) and liquid-bearing (bottom) layer persistence. The total number of cloud (liquid) samples in each month are shown by the triangle markers. The bars represent the longest-lived liquid-bearing cloud layers observed in each season (values are provided in the parentheses; dashed red line denotes 24 h).

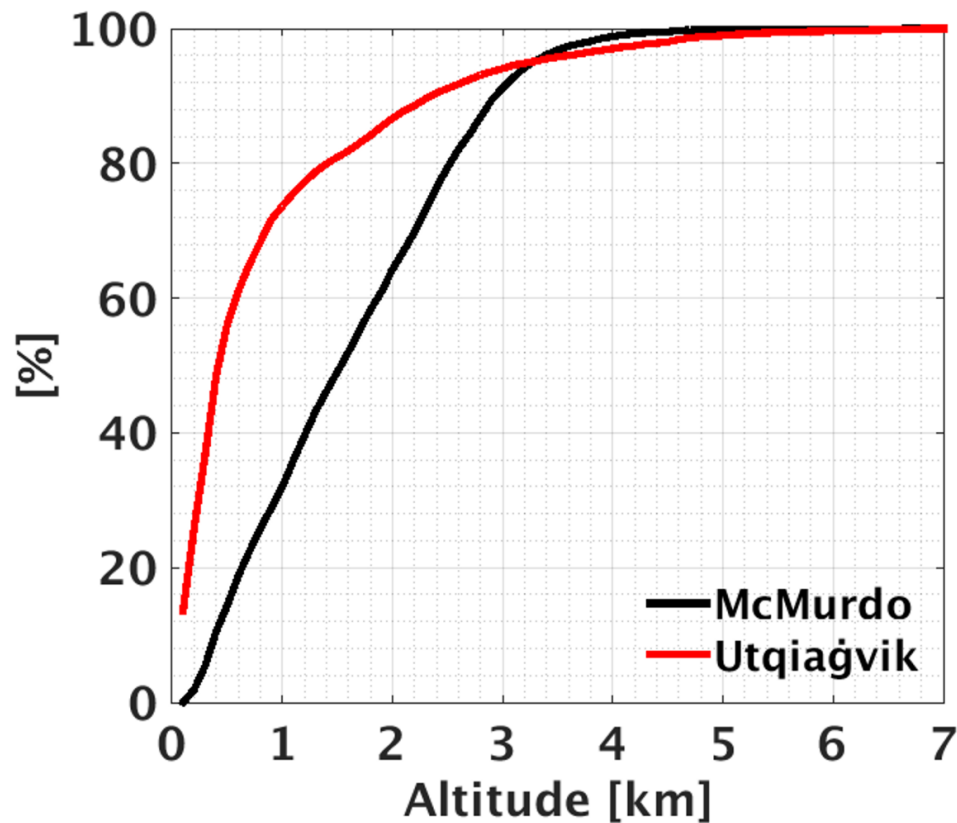
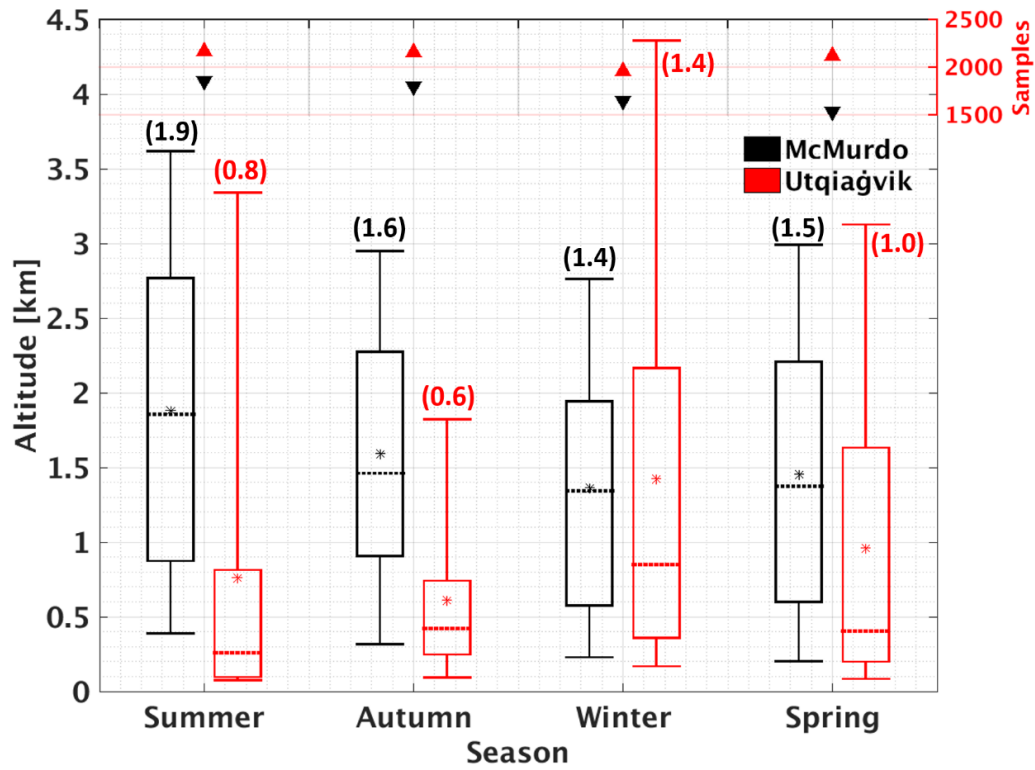


Figure 7. Lowest (per profile) liquid-bearing cloud layer base height box and whiskers diagram (top) and annual cumulative distribution function (bottom).

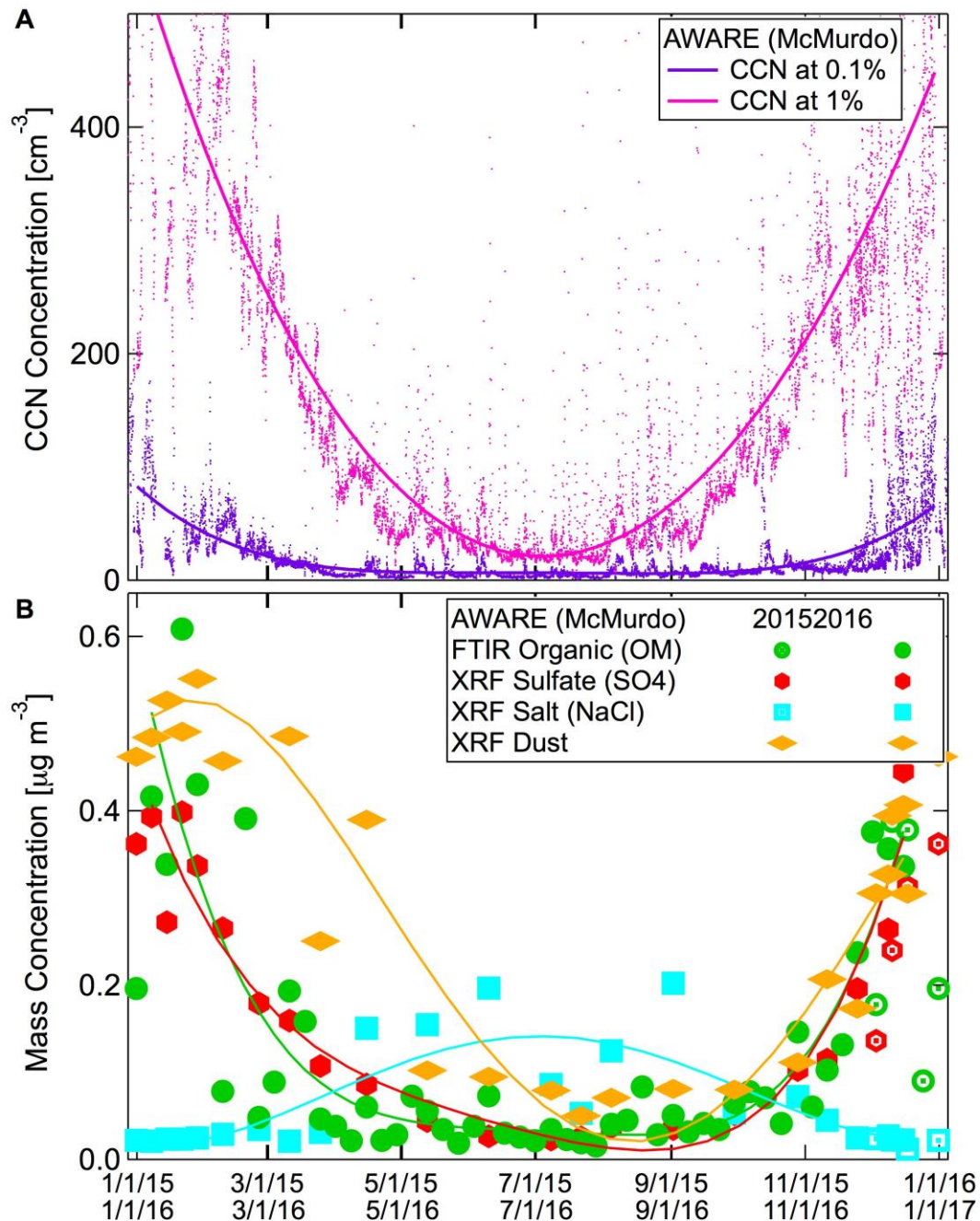


Figure 8. CCN and submicron aerosol particle mass concentrations during annual cycles measured at McMurdo Station, Antarctic: (A) CCN at 0.1% and 1% supersaturation and (B) organic, non-sea-salt sulfate (SO₄), sea salt, and non-sea-salt dust mass concentration (from Liu et al. 2018). Sea salt particle mass concentration was estimated as the sum of measured Na*1.47 and Cl based on Bates et al. 2009, and non-sea-salt sulfate (SO₄²⁻) mass concentration was scaled from XRF S after removing for sea-salt associated S (Liu et al. 2018). Non-sea-salt dust mass concentration was calculated from XRF metal concentrations, assuming dust consists of MgCO₃, Al₂O₃, SiO₂, K₂O, CaCO₃, TiO₂, Fe₂O₃, MnO, and BaO after removing sea-salt associated metal amounts (Liu et al. 2018). Lines show 5-parameter polynomial fits to 2016 measurements.

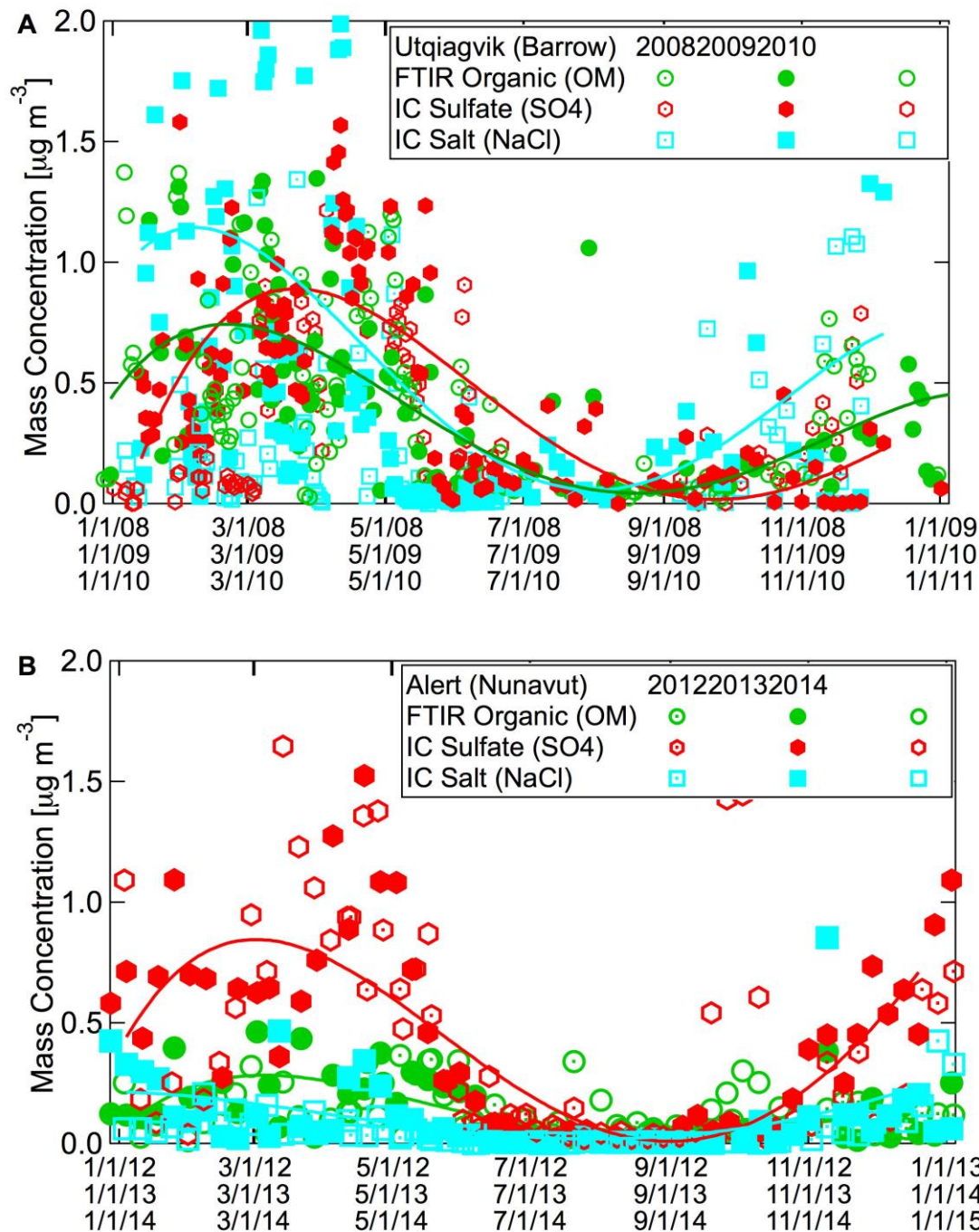


Figure 9. Submicron aerosol particle mass concentrations during annual cycles for the Arctic: (A) Organic, non-sea-salt sulfate (SO₄), and sea salt mass concentration measured at Utqiagvik, Alaska, by FTIR and IC (Shaw et al. 2010; Frossard et al. 2011; Quinn et al. 2002); (B) Organic, non-sea-salt sulfate (SO₄), and sea salt mass concentration measured at Alert, Nunavut, by FTIR and IC (Leaitch et al. 2018). Sea salt particle mass concentration was estimated as the sum of measured Na*1.47 and Cl based on Bates et al. 2012, and non-sea-salt sulfate (SO₄²⁻) mass concentration was calculated from IC sulfate after removing for sea-salt associated SO₄. Lines show 5-parameter polynomial fits to 2009 (Utqiagvik) and 2013 (Alert) measurements.

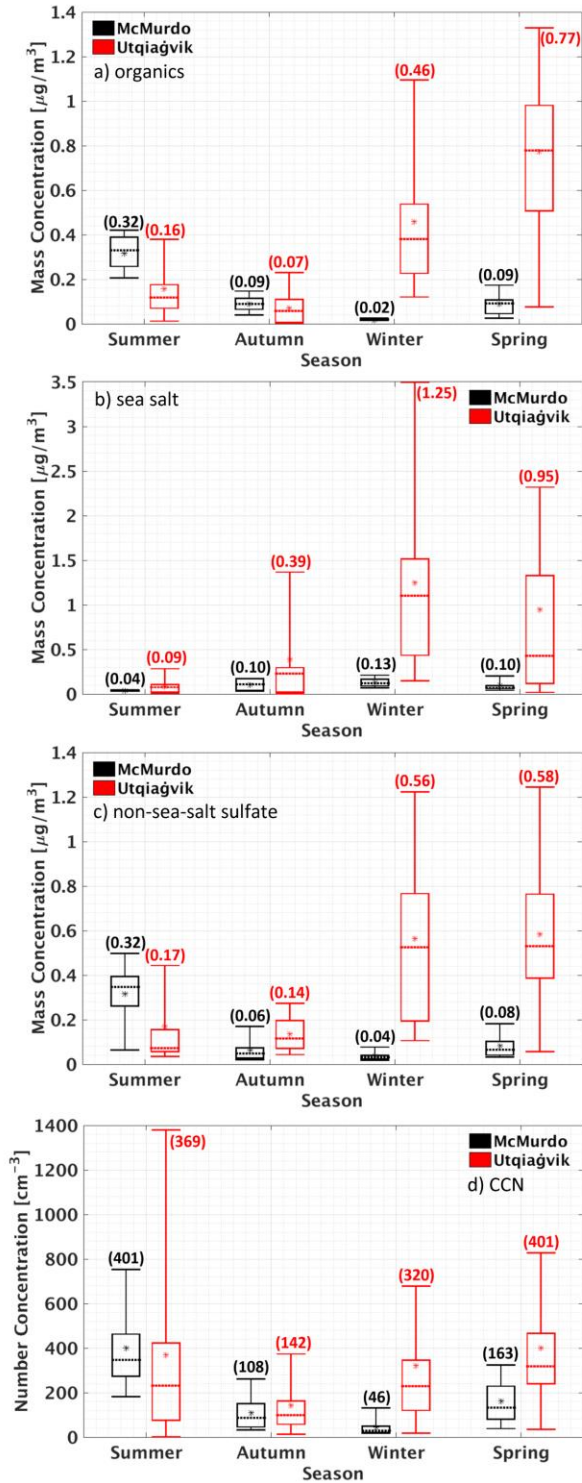


Figure 10. Box and whisker diagrams of submicron mass concentrations for (a) organic, (b) sea salt, and (c) non-sea salt sulfate, (d) CCN concentrations at 0.1% and 1%; designating the median (thick dotted line), 1st and 3rd quartiles (box edges), 5th and 95th percentiles (whiskers), and mean (asterisks). The McMurdo measurements are for 2016. The Utqiagvik mass and CCN concentrations are for 2009. The Utqiagvik CCN concentrations for 2009 were missing some supporting CN measurements so quality control was limited.

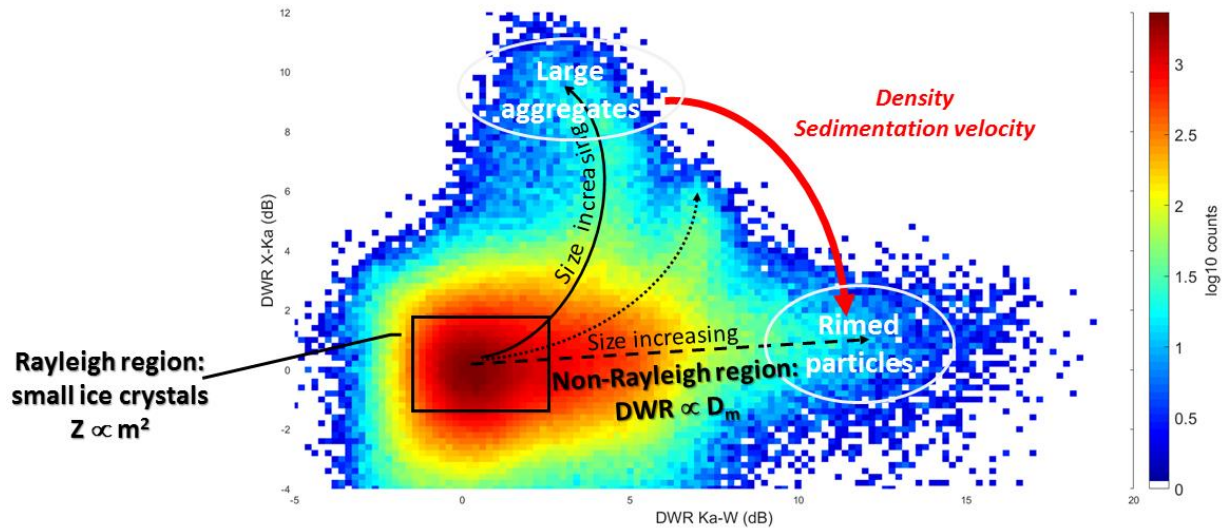


Figure 11. Two-dimensional histogram of DWR Ka-W versus DWR X-Ka measurements collected by the X-Ka and W-band ARM radars during 10 January 2016 at McMurdo Station. Negative DWRs are unexpected and might be caused by imperfect radar volume matching and measurement noise. Away from the Rayleigh region (black square) different growth regimes can be identified (continuous, dotted and dashed lines). The red arrow points towards ice particles characterized by higher densities and larger sedimentation velocities.

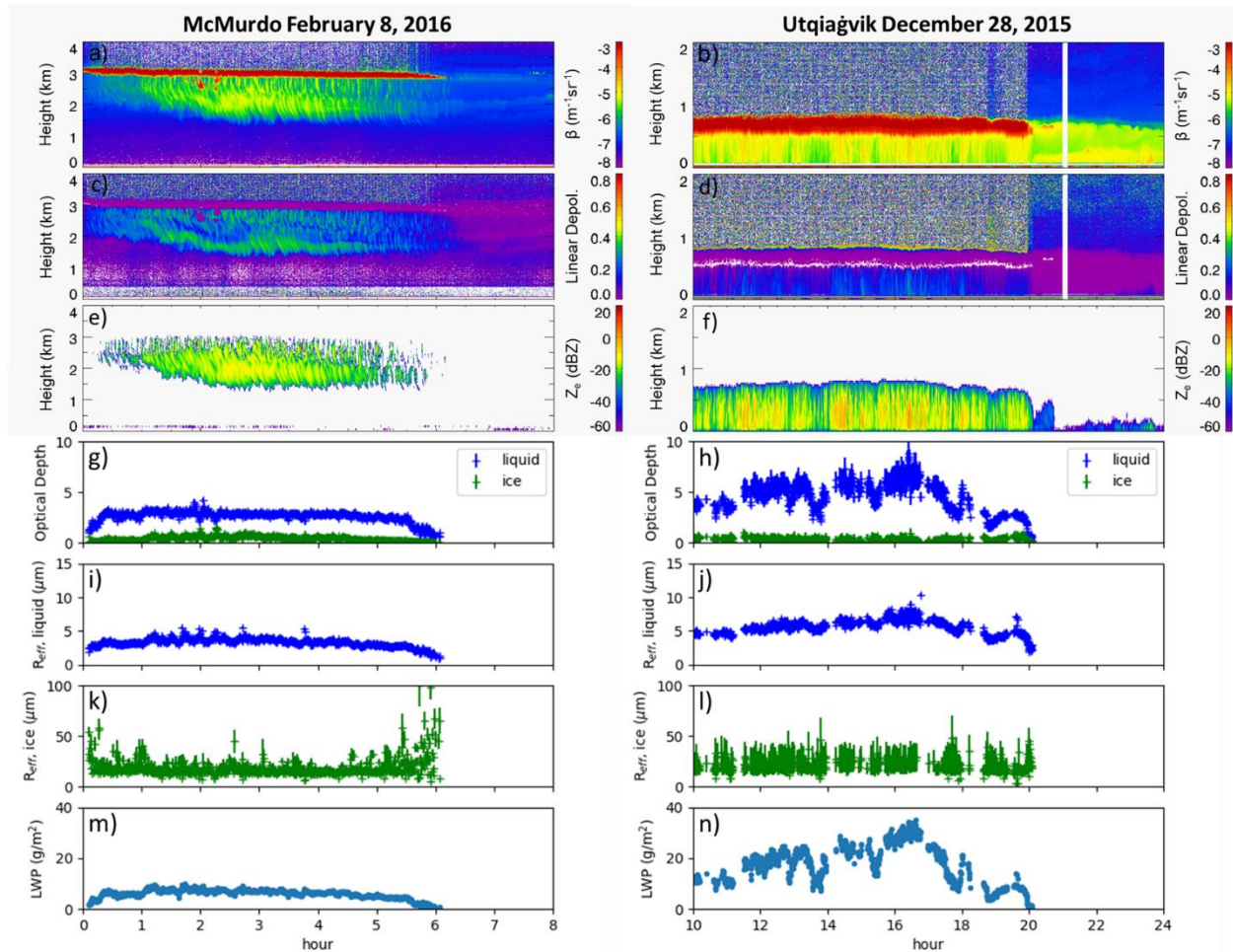


Figure 12. Multispectral characterization of mixed-phase clouds at McMurdo during AWARE (February 8, 2016) and at Utqiagvik, Alaska (December 28, 2015). Shown are time-height cross sections from zenith-pointing instruments: a,b) HSRL backscatter cross section (β), c,d) HSRL linear depolarization ratio, and e,f) Ka-band radar reflectivity (Z_e). Values for a-f are given by the color bars to the right of the panels. Panels g-m are retrievals of: g,h) optical depth (separately for ice and liquid phase), i,j) liquid water effective radius, k,l) ice particle effective radius, and m,n) liquid water path (LWP). The retrievals use downwelling infrared spectral radiances measured by the AERI via the method of Rowe et al. (2019, submitted, and references within). Retrieval uncertainty is indicated by the vertical extent of the symbols, obtained from the square root of the diagonal of the error covariance matrix for the state variable plotted.

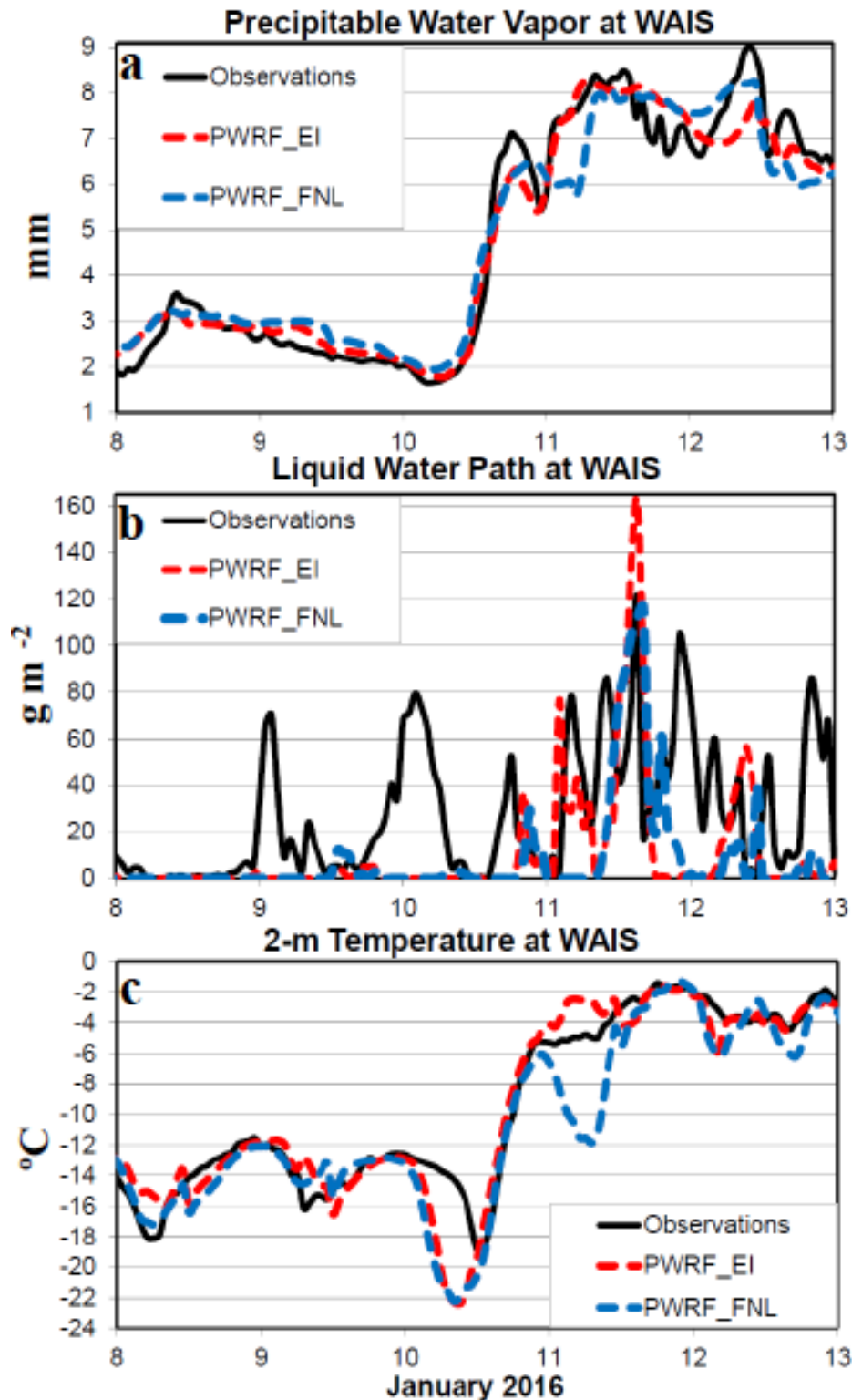


Figure 13. Simulation of the WAIS Divide melt event using Polar WRF (PWRF), using input from ERA-Interim (PWRF-EI) and GFS (PWRF-FNL), compared against AWARE observations from radiosondes and microwave radiometer measurements: (top) near surface (2-m) air temperature, (middle) cloud *LWP*, (bottom) vertically integrated *PWV*.

Figure 14. GCM evaluations at the WAIS Divide during the 2016 West Antarctic melt event for the DOE EAMv1 and GISS ModelE. EAMv1 simulations are run in hindcast mode (Ma et al. 2015) initialized using ERA5 with the 12-36 h hindcast period shown here. The GISS ModelE simulation is nudged to ERA5. The EAMv1 (red) and ModelE (blue) simulations are compared with observations (black) of (a) *PWV*, and (b) cloud *LWP*, both retrieved from surface microwave radiometer data. The primary warming period is indicated by gray shading. Model-observation differences for net surface fluxes are shown for (c) total net radiation (longwave plus shortwave), (d) total turbulence (sensible and latent heat, with the sign being positive towards the atmosphere), and (e) total energy into the snowpack. (f) Shows a scatter plot of the model-observation differences in net longwave flux at the surface (*LW*) versus differences in *LWP*. The observational data in (a)-(f) are described in Nicholas et al. (2017).

